Monthly Notices
of the
ROYAL ASTRONOMICAL SOCIETY

MNRAS **453,** 976–1001 (2015) doi:10.1093/mnras/stv1576

A spectroscopic survey of Herbig Ae/Be stars with X-shooter – I. Stellar parameters and accretion rates★

J. R. Fairlamb,[1]† R. D. Oudmaijer,[1] I. Mendigutía,[1] J. D. Ilee[2] and M. E. van den Ancker[3]

[1]*School of Physics and Astronomy, EC Stoner Building, University of Leeds, Leeds LS2 9JT, UK*
[2] *SUPA, School of Physics and Astronomy, University of St Andrews, North Haugh, St Andrews, Fife KY16 9SS, UK*
[3]*European Southern Observatory (ESO), Karl-Schwarzschild-Str. 2, D-85748 Garching, Germany*

Accepted 2015 July 13. Received 2015 July 13; in original form 2015 March 3

ABSTRACT

Herbig Ae/Be stars (HAeBes) span a key mass range that links low- and high-mass stars, and thus provide an ideal window from which to explore their formation. This paper presents Very Large Telescope/X-shooter spectra of 91 HAeBes, the largest spectroscopic study of HAeBe accretion to date. A homogeneous approach to determining stellar parameters is undertaken for the majority of the sample. Measurements of the ultraviolet are modelled within the context of magnetospheric accretion, allowing a direct determination of mass accretion rates. Multiple correlations are observed across the sample between accretion and stellar properties: the youngest and often most massive stars are the strongest accretors, and there is an almost 1:1 relationship between the accretion luminosity and stellar luminosity. Despite these overall trends of increased accretion rates in HAeBes when compared to classical T Tauri stars, we also find noticeable differences in correlations when considering the Herbig Ae and Herbig Be subsets. This, combined with the difficulty in applying a magnetospheric accretion model to some of the Herbig Be stars, could suggest that another form of accretion may be occurring within Herbig Be mass range.

Key words: accretion, accretion discs – techniques: spectroscopic – stars: early-type – stars: formation – stars: pre-main-sequence – stars: variables: T Tauri, Herbig Ae/Be.

1 INTRODUCTION

Herbig Ae/Be stars (HAeBes) are pre-main-sequence, PMS, stars that bridge the key mass range of 2–10 $M_{\odot}$, between low- and high-mass stars. Their importance lies in linking the reasonably well understood formation of low-mass stars, like the numerous classical T Tauri stars, CTTs (which have $M_{\star} < 2\,M_{\odot}$ and will go on to form stars like our own Sun), to the rarer, more deeply embedded high-mass stars (or massive young stellar objects, MYSOs). The greater number of HAeBes compared to forming high-mass stars, along with them being closer and optically visible, makes them a powerful link and important tool in furthering our understanding of star formation up to the high-mass star formation regime.

HAeBes were originally identified by Herbig (1960) in an attempt to push the mass boundaries in understanding of CTTs, and had to meet the criteria of: 'spectral type A or earlier with emission lines, lies in an obscured region, the star illuminates fairly bright nebulosity in its immediate vicinity'. The latter two criteria have been relaxed since then in order to find more potential targets (see Finkenzeller & Mundt 1984; Thé, de Winter & Perez 1994; Vieira et al. 2003). In these surveys, more attention has been drawn towards the colours of the objects, particularly in the infrared, IR. This is because the IR often displays an excess of emission, compared to main-sequence, MS, stars of the same spectral type, and is the product of the circumstellar disc around HAeBes. This has been confirmed in numerous studies (van den Ancker et al. 2000; Meeus et al. 2001), and by direct observations in the optical (McCaughrean & O'dell 1996; Grady et al. 2001), sub-mm (Mannings & Sargent 1997), and of scattered, polarized light (Vink et al. 2002, 2005). It is these indicators which ultimately point to the stars being young and in the PMS phase. This young nature, suspected by Herbig, was confirmed by Strom et al. (1972) who observed the HAeBes to have lower surface gravities than MS stars. With their PMS nature established, the next obvious questions are: what happens with the disc–star interaction; how do they both evolve; and what physical mechanisms are present in these interactions? And of course, how are these aspects related to each other between the CTTs and MYSOs?

With regard to the disc–star interaction, an ultraviolet, UV, excess in the CTTs (Garrison 1978; Gullbring et al. 1998) has been shown to match well with the theory of disc-to-star accretion within the

★ Based on observations using the ESO Very Large Telescope, at Cerro Paranal , under the observing programme 084.C-0952A.

† E-mail: pyjrf@leeds.ac.uk

magnetospheric accretion, MA, regime (Calvet & Gullbring 1998; Gullbring et al. 2000; Ingleby et al. 2013). Under this paradigm, the disc is truncated by the stellar magnetic field lines, and from here the material is funnelled by the field lines, in free-fall, on to the star. The accreted material shocks the photosphere causing X-ray emission, the majority of which is then absorbed by the surroundings, heating them, and is re-emitted at longer wavelengths, giving rise to an observable UV excess (Calvet & Gullbring 1998). Therefore, measurement of the UV excess can be directly related to accretion from the disc to the star. The accretion rate has large implications on PMS systems; it affects the achievable final mass of not just the star, but also any possible planets forming within the disc and the time-scales upon which they can evolve (Lubow & D'Angelo 2006; Dunhill 2015). Establishing an accretion rate also requires accurate stellar parameters which, until now, have mostly been performed on an ad hoc basis depending on the particular study. The results of this work will also help future studies to disentangle the complexities in the environments of these such as: outflows, infalling material, structure, and even possible ongoing planet formation.

However, for MA to be applicable, the star must have a magnetic field with sufficient strength to truncate the disc; for CTTs this is of the order of kilogauss (Ghosh & Lamb 1979; Koenigl 1991; Shu et al. 1994; Bouvier et al. 2007; Johns-Krull 2007). For MS stars, magnetic fields driven by convection are not predicted to exist for stars with $T_{\rm eff} > 8300$ K (Simon et al. 2002). However, this may not be the case for PMS stars as there have been a few detections of magnetic fields in HAeBes (Wade et al. 2005; Catala et al. 2007; Hubrig et al. 2009), but the origin of their fields remains unknown (be they dynamo generated or the result of fossil fields). The largest survey into the magnetic fields of HAeBes was performed recently by Alecian et al. (2013), and yields clear detections of only five stars out of 70. When applying the theory of MA (Koenigl 1991; Shu et al. 1994) to HAeBes, a weak dipole magnetic field of only a few hundred gauss, or even less, is needed for MA to occur (Wade et al. 2007; Cauley & Johns-Krull 2014). These strengths are below current detection limits, meaning that MA acting in HAeBes is still a possibility.

A key aim of this paper is to provide the largest survey on direct accretion tracers in HAeBes to date. To do this, measurements of the UV excess are made and fitted within the context of MA shock modelling. This method of accretion shock modelling has been successfully adapted and applied, in the majority of cases, to small sets of HAeBes in recent years (Muzerolle et al. 2004; Donehew & Brittain 2011; Mendigutía et al. 2011b, 2013, 2014; Pogodin et al. 2012). However, the number of HBes analysed in previous works is often small, particularly for early-type HBes, and needs to be tested further. The derivation of accretion rates, and other properties, depends heavily upon basic stellar parameters. Thus far, most works on accretion in HAeBes build upon previous stellar parameter determinations from a wide range of sources and methodologies. This can result in parameters which are not directly comparable within a sample. Therefore, our approach is to provide a homogeneous determination of stellar parameters for as many of the targets as possible. This not only helps in our accretion determination but also helps in future works which require basic stellar parameters, i.e. detailed modelling of the circumstellar disc or energy balance in the spectral energy distribution (SED).

The overall aim of this paper is to provide a quantitative look into the properties of HAeBes, with a particular emphasis on how the accretion rate varies as a function of stellar parameters, along with an assessment of the applicability of using MA to obtain the accretion rate. To do this, we present 91 HAeBe objects observed with the X-shooter spectrograph, Very Large Telescope (VLT), Chile. The paper is broken down into the following sections: Section 2 details the sample, observations, and data reduction; Section 3 details the methods, and results, of deriving the basic stellar parameters; Section 4 presents the methods of measuring the UV excess; Section 5 presents the derived accretion rates, including a detailed description of how MA is applied to the HAeBe sample; Section 6 forms the discussion; and Section 7 provides the conclusions of this work. Finally, photometric data and literature information on the sample are provided in Appendices A and B, respectively.

2 OBSERVATIONS AND DATA REDUCTION

2.1 X-shooter and target selection

Observations were performed over a period of 6 months between 2009 October and 2010 April using the X-shooter echelle spectrograph – mounted at the VLT, Cerro Paranal, Chile (Vernet et al. 2011). X-shooter provides spectra covering a large wavelength range of 3000–23 000 Å, split into three arms and taken simultaneously. The arms are split into the following: the UVB arm, 3000–5600 Å; the VIS arm, 5500–10 200 Å; and the NIR arm, 10 200–24 800 Å. The smallest slit widths available of 0.5, 0.4, and 0.4 arcsec were used to provide the highest possible resolutions of $R \sim 10\,000$, 18 000, and 10 500 for the respective UVB, VIS, and NIR arms. In total, 91 science targets were observed in nodding mode using an ABBA sequence. Table 1 includes details of each target's RA and Dec., exposure times, and the signal-to-noise ratio (SNR) in each arm. The SNR is calculated by analysing a 30 Å region of spectra centred about the wavelengths of 4600, 6750, and 16 265 Å for the UVB, VIS, and NIR arm, respectively. These regions were chosen as they are generally the flattest continuum regions in each star. Although emission lines, and absorption lines of cooler objects, can artificially lower the measured SNR, for a fair treatment we stick with the above regions to provide a rough guide to the quality of each spectrum.

The targets were selected from the catalogues of Thé et al. (1994) and Vieira et al. (2003). 51 targets were selected from Thé et al. (1994) and 40 from the Vieira et al. (2003) catalogue, bringing the total number of targets to 91. The observations cover around 70 per cent of the southern HAeBes identified by Thé et al. (1994) and about 50 per cent of the targets observed by Vieira et al. (2003). For many of these targets, little information is known about them, particularly in regard to multiplicity (see Duchêne 2015, for a review). It is known that HAeBes have high binary fractions (Baines et al. 2006; Wheelwright, Oudmaijer & Goodwin 2010), and as a consequence, any close separation binaries will contribute towards observed spectra. In this work, our focus is on the UV and optical portions of the spectra, where we assume that the primary star, the HAeBe target, provides the largest contribution to the brightness. Contributions from secondary stars will be greater in the observed literature photometry as they use either larger slit widths or an aperture greater than the slit widths used here. Photometry of all the targets are sourced from the literature, and are provided in Table A1 in Appendix A.

Telluric standards were observed either just before or after each science exposure. They were observed in stare mode for short exposures, ∼10 s, due to their brightness. Flux standard stars were observed on approximately half of the evenings in offset mode (offset mode allows accurate sky subtraction to be performed).

Table 1. Column 1 shows the target names, columns 2 and 3 are RA and Dec., column 4 gives the observation date, columns 5–7 give the exposure times for each arm, column 8 is the number of detector integration times for the NIR arm, and finally columns 9–11 give the signal-to-noise ratio in each arm.

Name	RA	Dec.	Obs date	Exposure time (s)				SNR		
	(J2000)		(yyyy/mm/dd)	UVB	VIS	NIR	NDIT	UVB	VIS	NIR
UX Ori	05:04:29.9	−03:47:16.8	2009-10-05	90 × 4	90 × 4	5 × 4	18	42	257	306
PDS 174	05:06:55.4	−03:21:16.0	2009-10-05	300 × 4	300 × 4	(20 × 6) × 4	2	127	64	225
V1012 Ori	05:11:36.5	−02:22:51.1	2009-10-05	250 × 4	(125 × 2) × 4	20 × 4	12	128	157	229
HD 34282	05:16:00.4	−09:48:38.5	2009-12-06	(15 × 2) × 4	(15 × 2) × 4	10 × 4	3	171	215	170
HD 287823	05:24:08.1	02:27:44.4	2009-12-06	(15 × 2) × 4	(15 × 2) × 4	15 × 4	2	99	171	256
HD 287841	05:24:42.8	01:43:45.4	2009-12-06	90 × 4	90 × 4	15 × 4	6	78	200	323
HD 290409	05:27:05.3	00:25:04.9	2010-01-02	(15 × 2) × 4	(15 × 2) × 4	15 × 4	2	195	157	130
HD 35929	05:27:42.6	−08:19:40.8	2009-12-17	(10 × 2) × 4	(10 × 2) × 4	5 × 4	8	36	125	161
HD 290500	05:29:48.0	−00:23:45.8	2009-12-17	150 × 4	150 × 4	75 × 4	2	208	341	331
HD 244314	05:30:18.9	11:20:18.2	2010-01-02	(15 × 2) × 4	(15 × 2) × 4	15 × 4	2	64	140	180
HK Ori	05:31:28.1	12:09:07.6	2009-12-17	250 × 4	250 × 4	20 × 4	12	49	120	192
HD 244604	05:31:57.3	11:17:38.8	2009-12-17	(15 × 2) × 4	(15 × 2) × 4	5 × 4	8	76	170	213
UY Ori	05:32:00.4	−04:55:54.6	2009-12-26	300 × 4	300 × 4	(50 × 6) × 4	1	229	326	143
HD 245185	05:35:09.7	10:01:49.9	2009-12-17	(15 × 2) × 4	(15 × 2) × 4	15 × 4	2	240	171	213
T Ori	05:35:50.6	−05:28:36.9	2009-12-17	(25 × 2) × 4	(25 × 2) × 4	(2 × 5) × 4	5	156	198	132
V380 Ori	05:36:25.5	−06:42:58.9	2009-12-17	(80 × 2) × 4	(80 × 2) × 4	(3 × 2) × 4	20	9	178	161
HD 37258	05:36:59.1	−06:09:17.9	2010-01-02	(15 × 2) × 4	(15 × 2) × 4	10 × 4	3	62	219	168
HD 290770	05:37:02.5	−01:37:21.3	2009-12-26	(15 × 2) × 4	(15 × 2) × 4	7 × 4	4	261	244	262
BF Ori	05:37:13.2	−06:35:03.3	2010-01-02	90 × 4	90 × 4	10 × 4	9	25	185	329
HD 37357	05:37:47.2	−06:42:31.7	2010-02-05	(10 × 2) × 4	(10 × 2) × 4	10 × 4	4	123	209	161
HD 290764	05:38:05.3	−01:15:22.2	2009-12-26	(30 × 2) × 4	(30 × 2) × 4	7 × 4	8	61	199	233
HD 37411	05:38:14.6	−05:25:14.4	2010-02-05	(25 × 2) × 4	(25 × 2) × 4	15 × 4	3	215	183	138
V599 Ori	05:38:58.4	−07:16:49.2	2010-01-06	360 × 4	(180 × 2) × 4	(10 × 2) × 4	10	61	149	328
V350 Ori	05:40:11.9	−09:42:12.2	2010-02-05	150 × 4	150 × 4	25 × 4	6	77	260	150
HD 250550	06:01:59.9	16:30:53.4	2010-01-02	(15 × 2) × 4	(15 × 2) × 4	3 × 4	10	103	218	200
V791 Mon	06:02:15.0	−10:01:01.4	2010-02-24	90 × 4	90 × 4	15 × 4	6	67	343	147
PDS 124	06:06:58.5	−05:55:09.2	2010-02-10	300 × 4	300 × 4	(50 × 6) × 4	1	188	62	119
LkHa 339	06:10:57.7	−06:14:41.8	2010-01-17	300 × 4	300 × 4	60 × 4	5	122	63	297
VY Mon	06:31:06.8	10:26:02.9	2010-02-08	(150 × 2) × 4	(100 × 3) × 4	(2 × 6) × 4	20	11	49	102
R Mon	06:39:10.0	08:44:08.2	2010-02-01	300 × 4	(150 × 2) × 4	(2 × 6) × 4	20	11	49	141
V590 Mon	06:40:44.7	09:47:59.7	2010-02-01	300 × 4	300 × 4	50 × 4	6	143	166	288
PDS 24	06:48:41.8	−16:48:06.0	2009-12-16	300 × 4	300 × 4	90 × 4	3	145	48	260
PDS 130	06:49:58.7	−07:38:52.1	2009-12-16	300 × 4	300 × 4	60 × 4	5	125	122	273
PDS 229N	06:55:40.1	−03:09:53.1	2010-02-10	300 × 4	300 × 4	100 × 4	3	111	105	191
GU CMa	07:01:49.6	−11:18:03.9	2009-12-16	(2 × 3) × 4	(2 × 3) × 4	(2 × 2) × 4	6	127	180	142
HT CMa	07:02:42.7	−11:26:12.3	2010-01-30	300 × 4	300 × 4	30 × 4	10	201	245	274
Z CMa	07:03:43.2	−11:33:06.7	2010-02-24	(75 × 2) × 4	(10 × 3) × 4	(0.665 × 5) × 4	20	28	87	102
HU CMa	07:04:06.8	−11:26:08.0	2010-01-17	300 × 4	300 × 4	50 × 4	6	185	218	217
HD 53367	07:04:25.6	−10:27:15.8	2010-02-24	(2 × 3) × 4	(2 × 3) × 4	(2 × 2) × 4	6	62	166	220
PDS 241	07:08:38.8	−04:19:07.0	2009-12-21	300 × 4	300 × 4	100 × 4	3	228	295	250
NX Pup	07:19:28.4	−44:35:08.8	2010-02-01	120 × 4	(60 × 2) × 4	(2 × 2) × 4	20	44	191	125
PDS 27	07:19:36.1	−17:39:17.9	2010-02-24	300 × 4	300 × 4	(2 × 6) × 4	20	9	118	228
PDS 133	07:25:05.1	−25:45:49.1	2010-02-24	300 × 4	300 × 4	(40 × 4) × 4	2	3	22	50
HD 59319	07:28:36.9	−21:57:48.4	2010-02-24	(10 × 2) × 4	(10 × 2) × 4	10 × 4	4	265	14	245
PDS 134	07:32:26.8	−21:55:35.3	2010-02-24	300 × 4	300 × 4	150 × 4	2	196	210	157
HD 68695	08:11:44.3	−44:05:07.5	2009-12-21	(20 × 2) × 4	(20 × 2) × 4	15 × 4	3	159	179	314
HD 72106	08:29:35.0	−38:36:18.5	2009-12-19	(10 × 2) × 4	(10 × 2) × 4	10 × 4	4	49	136	154
TYC 8581-2002-1	08:44:23.5	−59:56:55.8	2009-12-21	150 × 4	150 × 4	50 × 4	3	181	205	224
PDS 33	08:48:45.4	−40:48:20.1	2009-12-21	300 × 4	300 × 4	150 × 4	2	278	181	186
HD 76534	08:55:08.8	−43:27:57.3	2010-01-30	(10 × 3) × 4	(15 × 3) × 4	15 × 4	3	149	259	150
PDS 281	08:55:45.9	−44:25:11.4	2009-12-21	(15 × 2) × 4	(15 × 2) × 4	7.5 × 4	4	193	174	203
PDS 286	09:05:59.9	−47:18:55.2	2009-12-21	300 × 4	(150 × 2) × 4	(2 × 6) × 4	20	96	205	157
PDS 297	09:42:40.0	−56:15:32.2	2010-01-04	300 × 4	300 × 4	(150 × 2) × 4	2	213	210	188
HD 85567	09:50:28.3	−60:57:59.5	2010-03-06	(10 × 3) × 4	(15 × 3) × 4	2 × 4	20	142	183	283
HD 87403	10:02:51.3	−59:16:52.7	2010-03-06	(15 × 2) × 4	(15 × 2) × 4	15 × 4	2	137	137	160
PDS 37	10:10:00.3	−57:02:04.4	2010-03-31	300 × 4	300 × 4	(3 × 6) × 4	15	18	182	166
HD 305298	10:33:05.0	−60:19:48.6	2010-03-31	90 × 4	90 × 4	45 × 4	2	155	209	207
HD 94509	10:53:27.2	−58:25:21.4	2010-02-05	(20 × 2) × 4	(20 × 2) × 4	15 × 4	3	12	171	208
HD 95881	11:01:57.1	−71:30:46.9	2010-01-04	(10 × 3) × 4	(15 × 3) × 4	2 × 4	20	56	223	296
HD 96042	11:03:40.6	−59:25:55.9	2010-02-05	(10 × 2) × 4	(10 × 2) × 4	10 × 4	4	97	107	176
HD 97048	11:08:03.0	−77:39:16.0	2010-02-05	(15 × 3) × 4	(15 × 3) × 4	2 × 4	20	208	254	200

Table 1 – *continued.*

Name	RA (J2000)	Dec. (J2000)	Obs date (yyyy/mm/dd)	Exposure time (s) UVB	VIS	NIR	NDIT	SNR UVB	VIS	NIR
HD 98922	11:22:31.5	−53:22:09.0	2010-03-30	(3 × 3) × 4	(3 × 3) × 4	(0.75 × 2) × 4	20	85	196	103
HD 100453	11:33:05.3	−54:19:26.1	2010-03-29	(10 × 3) × 4	(15 × 3) × 4	2 × 4	20	35	110	289
HD 100546	11:33:25.1	−70:11:39.6	2010-03-30	(3 × 3) × 4	(3 × 3) × 4	(1 × 2) × 4	20	283	206	348
HD 101412	11:39:44.3	−60:10:25.1	2010-03-30	(15 × 2) × 4	(15 × 2) × 4	10 × 4	3	89	125	169
PDS 344	11:40:32.8	−64:32:03.0	2010-03-31	300 × 4	300 × 4	150 × 4	2	236	190	157
HD 104237	12:00:04.8	−78:11:31.9	2010-03-30	(3 × 3) × 4	(3 × 3) × 4	(0.75 × 2) × 4	20	25	88	216
V1028 Cen	13:01:17.6	−48:53:17.0	2010-03-29	90 × 4	90 × 4	10 × 4	9	101	165	148
PDS 361S	13:03:21.6	−62:13:23.5	2010-03-31	300 × 4	300 × 4	150 × 4	2	118	192	181
HD 114981	13:14:40.4	−38:39:05.0	2010-03-29	(3 × 3) × 4	(3 × 3) × 4	(3 × 2) × 4	6	250	185	82
PDS 364	13:20:03.5	−62:23:51.7	2010-03-31	300 × 4	300 × 4	90 × 4	3	130	116	168
PDS 69	13:57:44.0	−39:58:47.0	2010-03-29	(15 × 2) × 4	(15 × 2) × 4	5 × 4	6	45	66	149
DG Cir	15:03:23.4	−63:22:57.2	2010-03-31	360 × 4	(180 × 2) × 4	10 × 4	20	14	103	138
HD 132947	15:04:56.2	−63:07:50.0	2010-03-12	(20 × 2) × 4	(20 × 2) × 4	15 × 4	3	232	265	236
HD 135344B	15:15:48.2	−37:09:16.7	2010-03-31	(5 × 2) × 4	(5 × 2) × 4	2 × 4	6	42	116	307
HD 139614	15:40:46.3	−42:29:51.4	2010-03-28	(10 × 2) × 4	(10 × 2) × 4	5 × 4	8	35	139	127
PDS 144S	15:49:15.4	−26:00:52.8	2010-03-31	300 × 4	300 × 4	(5 × 5) × 4	10	49	127	124
HD 141569	15:49:57.8	−03:55:18.6	2010-03-28	(2 × 3) × 4	(2 × 3) × 4	(2 × 2) × 4	6	177	151	144
HD 141926	15:54:21.5	−55:19:41.3	2010-03-12	(15 × 2) × 4	(15 × 2) × 4	3 × 4	10	66	198	78
HD 142666	15:56:40.2	−22:01:39.5	2010-03-28	(15 × 3) × 4	(15 × 3) × 4	2 × 4	20	53	126	114
HD 142527	15:56:41.8	−42:19:21.0	2010-04-01	(5 × 2) × 4	(5 × 2) × 4	1 × 4	20	23	88	305
HD 144432	16:06:57.8	−27:43:07.4	2010-03-12	(10 × 3) × 4	(15 × 3) × 4	2 × 4	20	55	126	109
HD 144668	16:08:34.0	−39:06:19.4	2010-03-30	(3 × 3) × 4	(3 × 3) × 4	(0.75 × 2) × 4	20	96	191	276
HD 145718	16:13:11.4	−22:29:08.3	2010-03-29	(15 × 2) × 4	(15 × 2) × 4	3 × 4	10	85	165	165
PDS 415N	16:18:37.4	−24:05:22.0	2010-03-31	300 × 4	300 × 4	(10 × 5) × 4	5	13	66	103
HD 150193	16:40:17.7	−23:53:47.0	2010-03-30	(25 × 3) × 4	(15 × 3) × 4	2 × 4	20	100	152	322
AK Sco	16:54:45.0	−36:53:17.1	2009-10-05	(10 × 2) × 4	(10 × 2) × 4	5 × 4	8	26	91	198
PDS 431	16:54:58.9	−43:21:47.7	2010-04-01	300 × 4	300 × 4	150 × 4	2	174	171	84
KK Oph	17:10:07.9	−27:15:18.6	2010-03-26	200 × 4	(100 × 2) × 4	(2 × 6) × 4	20	58	274	231
HD 163296	17:56:21.4	−21:57:21.7	2009-10-05	(3 × 3) × 4	(3 × 3) × 4	(1 × 2) × 4	20	87	241	127
MWC 297	18:27:39.7	−03:49:53.1	2009-10-06	300 × 4	10 × 4	(0.665 × 15) × 4	20	162	96	127

2.2 Data reduction

All data were reduced following standard procedures of the X-shooter pipeline v0.9.7 (Modigliani et al. 2010). Only one aspect is not included in the standard procedures and that is flux calibration. However, we do not require a flux calibration for the work presented in this paper, we focus instead on determining the spectral shape. This spectral shape is needed in the UVB arm, specifically across the Balmer jump region where the difference between the *U* band and *B* band is required in order to measure any excess UV emission. The analysis of the spectral lines and the derivation of their luminosities are deferred to Paper II.

Ordinarily, to obtain the correct spectral shape, a flux calibration is performed using the observed flux standards of each night. However, as mentioned, flux standards were not observed on all evenings. A solution to this is to instead use the telluric standards, for which there is at least one per target, as a means of correction. This will ensure a uniform treatment to all of the targets. Caution should be noted of using non-flux standard stars for calibration; to mitigate any problems that could arise from this, consistency checks are made against the flux standards for the nights where they are available and will be discussed at the end of this section. For this method of spectral shape calibration, accurate knowledge of the spectral type of each telluric is required. To ensure a homogeneous reduction, we adopted our own spectral typing of each telluric in this work. This helps to minimize any reduction errors, and will also allow us to place a systematic error on this reduction method. Full details of the spectral typing, along with a discussion of how they compare with literature values, will be provided in Section 3.

Once the spectral type is determined, the observed telluric spectrum is divided through by a model atmosphere of the same spectral type in order to obtain an instrumental *response* curve. The model atmospheres adopted here, and throughout this work, are sets of Kurucz–Castelli models (Kurucz 1993; Castelli & Kurucz 2004) computed by Munari et al. (2005), due to their small dispersion of 1 Å over the UVB wavelength range (these will be referred to as KC-models hereafter). The resulting response curve from this division is then fitted with two curves: one for the echelle orders where $\lambda < 3600$ Å and another for the orders where $\lambda > 3600$ Å. This is because the response at ∼3600 Å is not the same between the two overlapping echelle orders. Fig. 1 shows the procedure of the above method, for a target star for which both flux standard and telluric standards were observed, and highlights the two different response curves intersecting around the *U*-band region in the middle panels. The figure also provides a consistency check by comparing the flux standard reduction, on the left, to the telluric standard reduction, on the right. The bottom panel of the figure demonstrates the similarity of both results with a difference of <3 per cent across the spectra. Larger deviations are seen between the two spectra close to 3000 Å, due to low levels of counts. This region is not used in this work and can be disregarded. This same check is performed on other stars for which both a telluric and flux standard are available, and the maximum deviation observed is only 5 per cent across the spectra. Overall, it can be seen that this method of using the telluric for instrumental response correction provides a satisfactory calibration of the data, and is therefore performed on all targets.

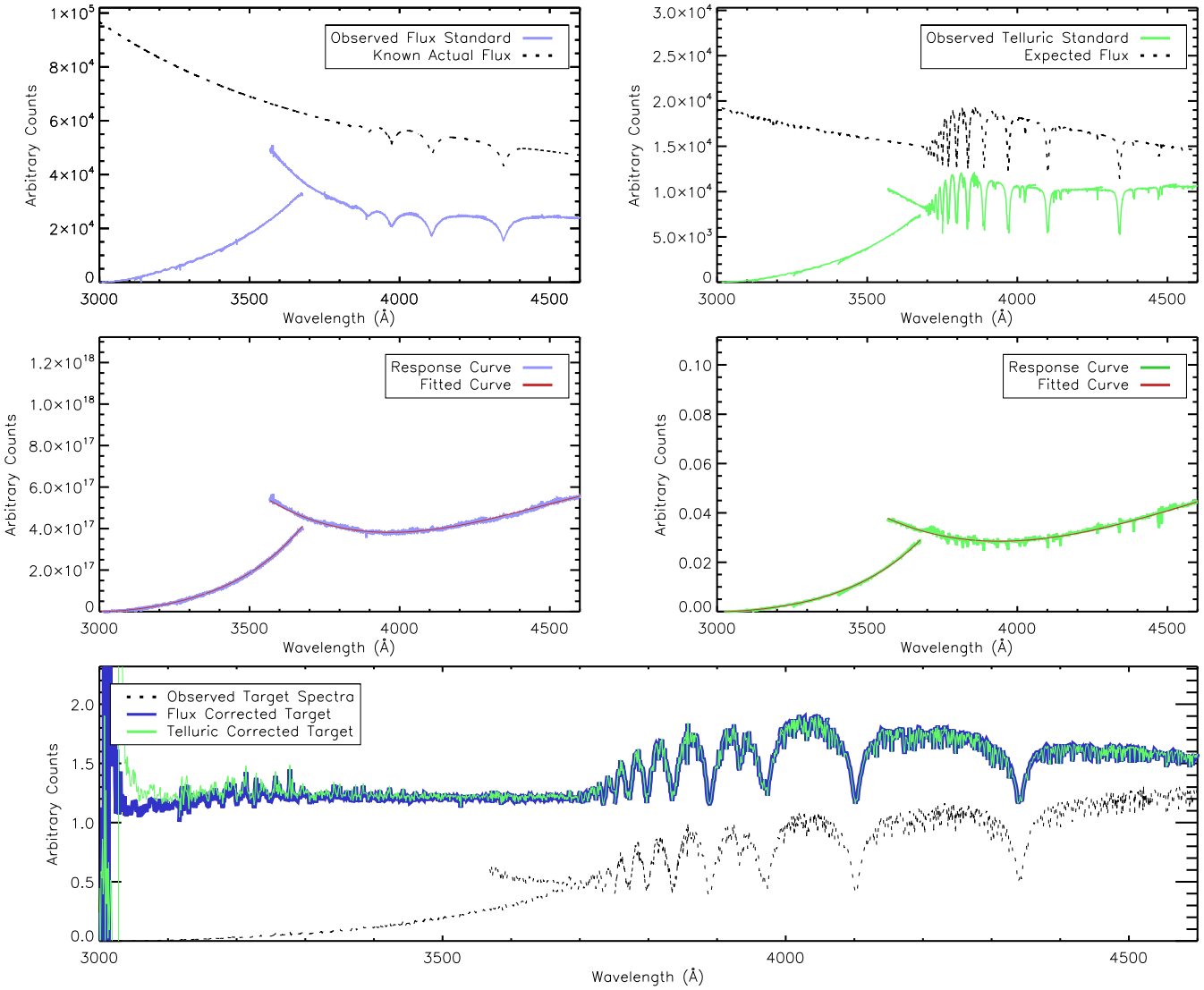

Figure 1. The two different cases of correcting target spectra via either a flux standard (shown on the left) or a telluric standard (shown on the right). The top-left panel shows the observed flux standard (blue) and the true flux of the standard star (dashed black). Similarly, the top-right panel shows the observed telluric standard (green) and its expected spectra (dashed black). The middle two panels show a division of the observed standard stars by their expected spectra from the top panels (blue and green). A two-part curve (red) is also shown as a fit to this division. The bottom panel shows the result of applying the two fits from the middle panel to the target spectra (dashed black). It can be seen that the two methods of correction are equivalent by lying on top of each other. All spectra have been arbitrarily scaled in order to be visible on each plot.

3 DETERMINING THE DISTANCE AND STELLAR PARAMETERS

Determining accurate stellar parameters is crucial for extracting an accretion rate, and for obtaining further information about the age, evolution, and ongoing processes in the environment around HAeBe stars. Many stars in this sample have had their stellar parameters determined previously, but this has often been done in smaller subsets using a variety of methods (Mora et al. 2001; Hernández et al. 2004; Manoj et al. 2006; Montesinos et al. 2009; Alecian et al. 2013, see also Appendix A for additional references). For this reason, a full treatment of determining stellar parameters is performed on the entire sample, in a homogeneous fashion, to provide better consistency between the stars. A comparison will also be made with the literature values to confirm the method employed, as most stars would be expected to have similar temperatures to the previous literature values.

The determination of parameters is performed in a three-step process. (1) Spectral typing is performed using the X-shooter spectra to provide accurate limits on the effective surface temperature, $T_{\rm eff}$, and where possible the surface gravity too, $\log(g)$. (2) KC-models and the photometry are used to assess the reddening, A_V, and distance/radius, $D/R_\star$, ratio towards the targets. (3) Finally, PMS evolutionary tracks are used to infer a mass, $M_\star$, and age (and other parameters if not determined yet). The stages of this process are now given in detail.

3.1 Temperature and surface gravity determination

The first stage takes advantage of the large wavelength coverage and good spectral resolution of X-shooter to perform spectral typing, allowing us to narrow down the possible $T_{\rm eff}$ and $\log(g)$ of each target. This is done by following a similar method to Montesinos

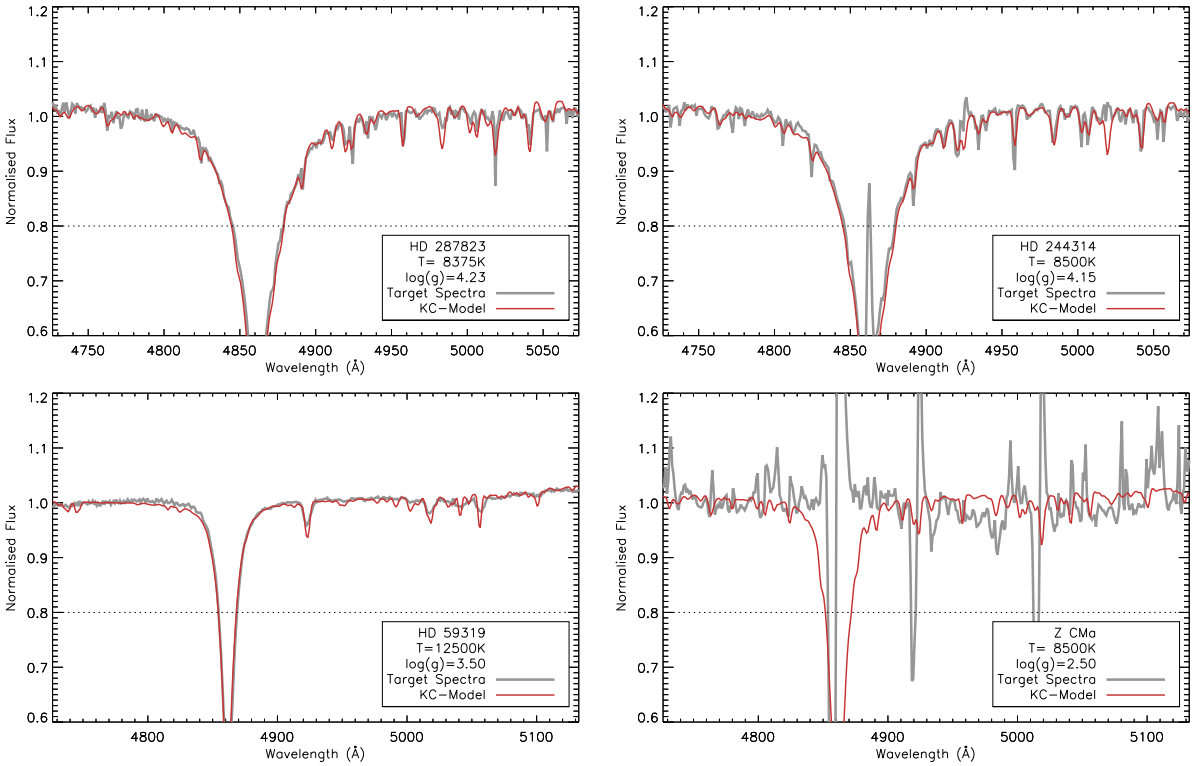

Figure 2. Examples of spectral typing for four targets are presented here. Each panel shows both the target spectra (grey) and a KC-model which denotes a good fit (red). The parameters for the KC-model are given for each fit. Also plotted is a dashed line, at 0.8 of the normalized intensity, which is used as a cut-off in the fitting. The two panels on the left show the cases for straightforward fit where there is no obvious emission. The figure in the top right is a case where there is clear emission present; a good fit is still achieved. The bottom-right panel gives an example of one of the few objects which cannot be spectrally typed in this way due to extremely strong emission; this exceptional object, and others like it, is presented in detail in Appendix B.

et al. (2009), of spectral typing using the wings of the hydrogen Balmer series, and the continuum region 100–150 Å either side of the lines. These lines are favoured due to their sensitivity to changes in $T_{\rm eff}$ and $\log(g)$. Specifically, the Hβ, Hγ, and Hδ lines are used as they have the largest intrinsic absorption of the series, except for the Hα line. Hα is not used for spectral typing as it is often seen entirely in emission, with the emission being both the strongest and broadest of the Balmer series in HAeBes. This could in turn affect the derived parameters. Therefore, fitting of models to the line wings is performed using the other lines in the series. To perform the fitting, each line is first normalized based on the continuum either side of the line. They are then compared against a grid of KC-model spectra, which have also been normalized in the same way using the same regions either side of the line. The resolution of the grid is set to be in steps of 250 K for $T_{\rm eff}$ and 0.1 dex in $\log(g)$. The metallicity is kept at $[M/{\rm H}] = 0$ throughout, although it has been shown that the choice of metallicity can affect spectral typing in HAeBes (Montesinos et al. 2009). The fit of the synthetic spectra to the observed spectra is judged using the wings of each line and continuum features, where the intensity is greater than 0.8; the line centre is excluded as it can often be found in emission. This approach avoids the problems of both emission and rotational broadening in the line. Fig. 2 gives four examples of this fitting, highlighting the power for obtaining an accurate $T_{\rm eff}$ and $\log(g)$, where many errors are as small as the chosen step size. However, despite this reliable technique, issues arise for two cases. The first is that there is a non-linear relationship between the Balmer line width and the surface gravity for objects which have $T_{\rm eff} < 8000$ K (Guimarães et al. 2006). However, for temperatures up to 9000 K, there is increased uncertainty due to the large presence of absorption features, which make normalizing and comparing different surface gravity scenarios increasingly difficult. For these reasons, we do not constrain $\log(g)$ using the spectra for stars with a suspected $T_{\rm eff} < 9000$ K.

The widths of the Balmer lines are tightly correlated to $T_{\rm eff}$ and $\log(g)$, to the point where different combinations of the two can produce the same widths. However, this degeneracy can be broken when viewing the whole of the line profile and the absorption features within them (and also the photospheric absorption features outside the wings).

The second issue concerns objects which display very strong emission lines, where the line strength is exceptionally strong across the Balmer series to the point where the widths of the lines eclipse even the broad photospheric absorption wings. Extremely strong P-Cygni, or inverse P-Cygni, profiles can also affect the line shape in the wings. An example of extreme emission is shown in the bottom-right panel of Fig. 2, where none of the intrinsic photospheric absorption lines can be seen due to the emission. P-Cygni absorption is also present in this example further complicating any possible analysis of the wings. Objects, like the example just given, where both $T_{\rm eff}$ and $\log(g)$ cannot be constrained by this method, will be treated separately on an individual basis and are detailed in Appendix B. The objects for which $T_{\rm eff}$ has been constrained can have all of their parameters determined in the next two steps.

For the telluric standards, the same above steps are applied. This is because they are well-behaved stars for which a $T_{\rm eff}$ and $\log(g)$ determination is straightforward. These parameters are required for the data reduction discussed previously in Section 2.2.

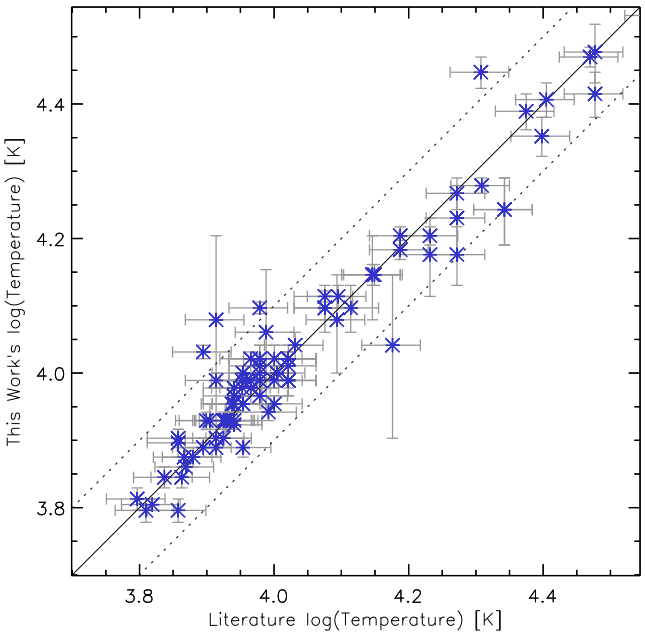

Figure 3. The temperatures derived in this work in comparison to literature estimates. The solid black line is the expected line of correlation and the dashed lines are a 0.1 dex deviation from this. The standard deviation between the two is only 0.02, with a mean offset of 0.03 towards this work. The dashed lines therefore encompass 3σ, showing that the two samples are well correlated. The literature temperatures used and their references are provided in Appendix A.

Fig. 3 compares the temperatures derived in this work against previous estimates from the literature (see Table A1 in Appendix A). The temperature is chosen for comparison as it is a key stellar parameter which can be determined more readily than log(g), and its appearance in the literature is more frequent than other parameters (allowing a greater number of comparisons to be made). The majority of literature works provide a spectral type rather than a precise temperature, so we assign an error of 10 per cent for these. The figure shows that over 95 per cent of the stars are in agreement, within the errors. Also, the temperature determinations in this work have been based on some of the best spectra available for these objects, which help keep errors to a minimum. This serves as a justification for the homogeneous approach to determining temperatures and their use here, for both the target stars and the telluric standards alike.

3.2 Photometry fitting

The second step of this process takes two directions. One case is where both $T_{\rm eff}$ and log(g) could be determined from the spectra, and the other case is for when only $T_{\rm eff}$ could be determined. In both cases, fitting spectra of model atmospheres, based on the parameters determined in the previous step, to the observed optical photometry will be performed. The fitting will provide a level of reddening, A_V, to each star and a scaling factor, $D/R_\star$, due to the fitting of surface flux models to observed photometry. An accurate temperature is paramount here in order to break any degeneracy of fitting models to the photometry.

To perform the fitting only the *BVRI* points are used; the *U* band can be influenced heavily by the Balmer excess, and no photometry longwards of the *I* band is used due to the possible influence of the IR excess (which itself would require dedicated modelling). The *B* band can also be affected in the cases of extremely large flux excess. Fortunately, these cases are rare and the change in the *B*-band magnitude would not significantly affect the fitting (the fitting is far more sensitive to the input temperature).

Another point to consider when looking at optical photometry is the effects of variability, as this has been observed in numerous HAeBes (de Winter et al. 2001; Oudmaijer et al. 2001; Mendigutía et al. 2011a, 2013; Pogodin et al. 2012). However, variability information is not present for all of the targets, but we estimate that the calculated parameters will not be affected significantly if the photometric variation is less than 0.2 mag. In all cases, we use photometry when at maximum brightness, as this best reflects the scenario where we are mostly viewing the stellar photosphere. So an assumption is adopted here that the photometry we use is predominately photospheric and not highly variable.

In order to fit the photometry, a unique grid of KC-models is set up based on the limits derived in step 1 for each star; the grid follows the same step sizes used in the previous step too. Log(g) does not have a significant effect on the fitting to the photometry, as the spectral shape is overwhelmingly dominated by the temperature. This allows log(g) = 4.0 to be adopted and used in this step for the stars where log(g) could not be determined from the spectra; this value will be revised in the next step.

The models are reddened until a best fit to the photometry is achieved, the best fit being when the reddened SED shape of the model is in line with the photometry. The dereddening is performed using the reddening law of Cardelli, Clayton & Mathis (1989), with a standard $R_V = 3.1$, in all cases. It is possible that the total-to-selective extinction may be higher, possibly $R_V = 5.0$, for some of the stars in this sample based on previous analysis of HAeBes (Hernández et al. 2004; Manoj et al. 2006). However, the choice of R_V will only affect the targets with the most extinction and the changes this will have on the stellar parameters and accretion rates are minimal due to the observed colour excess remaining the same. The majority of the targets have a mean $E(B-V) \approx 0.4$.

Returning to the fitting, the model is normalized to the *V*-band point by a scaling factor, which is $(D/R_\star)^2$. This scaling factor arises from the fitting of models in units of surface flux to observed photometry. An advantage of knowing this scaling factor is that it allows either distance or radius to be determined provided the other is known. Fig. 4 shows an example of the above fitting for the case of V1012 Ori, along with a dereddened version of the photometry and the model spectra. This object is shown as it demonstrates a clear IR excess, a noticeable A_V, and a *U*-band magnitude slightly higher than the KC-model spectra (possible Balmer excess).

At this stage, the techniques diverge between the stars for which a log(g) was determined and for the ones in which it could not be. For the former, no further action is taken in this step. For the latter, a distance is adopted to the star based upon the location of the star on the sky and its possible associations with nearby star-forming regions. The stars for which this is performed are noted in Table 2; the literature distances adopted and references are both provided in the same table (and also in Table A1 in Appendix A). An error of 20 per cent is adopted for the distance, as this helps reflect the additional uncertainty on whether the star is truly part of the association, and the possible extent of the association. If the error is higher than 20 per cent, then the higher error is adopted instead. By adopting a distance to these stars, a radius can be determined from the scaling factor. Then, combining this radius with the temperature, the luminosity is calculated by a blackbody relationship of $L_\star = 4\pi R_\star^2 \sigma T_{\rm eff}^4$ (this calculation is equivalent to the sum of the flux under the KC-model multiplied by $4\pi D^2$).

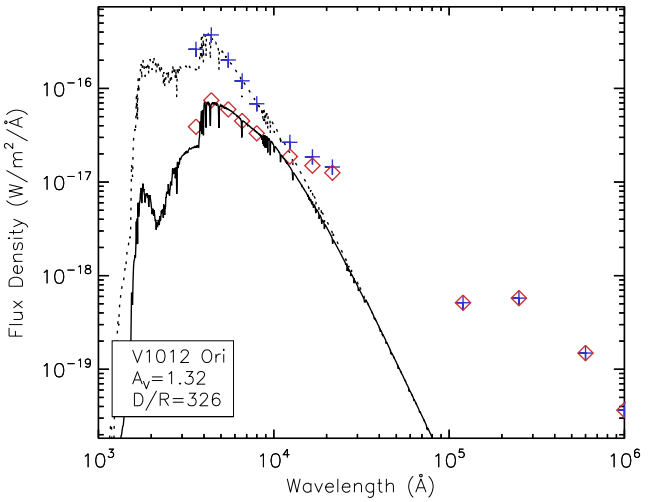

Figure 4. Here is an example of step 2 in the stellar parameter determinations (see Section 3.2), where a reddened KC-model (black) is fitted to the observed photometry (red diamonds). The opposite is also shown, of dereddened photometry (blue plus signs) fitted to a KC-model with no reddening applied (dashed line). The level of reddening, A_V, is displayed in the figure. The fit provides a ratio between the distance to the star and its radius, $D/R_\star$, as this is required to scale the model to fit the photometry. Also visible in this plot is how the *U*-band magnitude is higher than the KC-model used, a possible indication of Balmer excess. A clear IR excess can also been seen, starting at around the *J* band, a typical feature of PMS stars.

3.3 Mass, age, radius, and log(*g*) determination

In this third and final step, the remaining stellar parameters are now determined through the use of PMS tracks. The PARSEC tracks of Bressan et al. (2012) are used for the majority of this step as they cover a mass range of 0.1–12 $M_\odot$, which encompasses all of the theoretical HAeBe mass range, and a metallicity is chosen of $Z = 0.01$ (this is close to solar metallicity; Caffau et al. 2011). Additionally, two tracks from Bernasconi & Maeder (1996) are used for objects greater than 12 $M_\odot$. Each track is of a fixed mass, with no accretion contribution, which evolves over time in $T_{\rm eff}$ and $L_\star$ as the star contracts. As $T_{\rm eff}$ and $L_\star$ change so do $R_\star$ and log(g) as a consequence. This allows each star to be plotted on either an $L_\star$ versus $T_{\rm eff}$ set of tracks, for the stars where $L_\star$ is known from the adopted distance, or on a log(g) versus $T_{\rm eff}$ set of tracks, for the stars where both log(g) and $T_{\rm eff}$ were determined from the spectra. For the first scenario, a mass and an age are extracted from the PMS tracks. Then, log(g) is calculated using this mass and the radius from the previous step. For the second scenario, luminosity, mass, and age are all extracted from the tracks. These can then be used to obtain a radius from the temperature and luminosity, or the mass and log(g), both choices are equivalent. Finally, using the $D/R_\star$ factor, a distance can be determined.

However, not all cases allow parameters to be extracted from the tracks. These few cases are where the stars are located below the zero-age main sequence, ZAMS. It should be noted that for a few of these cases, where the stars are only just below the ZAMS of the chosen tracks, then tracks relating to stars with a lower metallicity may be more appropriate. However, in general, it appears more likely that their placement is genuinely below the ZAMS and is due to the adopted literature distances used being incorrect, as their use provides small radii from the $D/R_\star$ ratio. The radius is deemed too small as it is less than the expected radius of a ZAMS star of the same temperature. Additionally, most of these stars have diffuse interstellar bands, DIBs, in their spectra which suggest $A_V \sim 0.5$–2.0 mag (Jenniskens & Desert 1994). Extinction due to DIBs follows a trend of ∼1.8 mag kpc^{-1} (Whittet 2003). This suggests that the distances should be greater than the adopted values and should be revised. Previously, for these stars, the assumption had been made that the stars are associated with a star-forming region. It is now more probable from the spectral typing and position of the stars in relation to the PMS tracks that some of the distances chosen are not valid, i.e. the star may not be associated with the chosen region. Also, the spectrally determined $T_{\rm eff}$ is more likely to be correct as it comes from spectra which have been directly observed from the star itself, opposed to a distance inferred from a possible association. A solution to this problem is calculating new distances to these outlier targets, ones which provide more sensible radii and agree with the spectrally determined temperature. To do this, the stars are placed on the ZAMS at a point appropriate for their derived temperature; essentially, this is a lower limit to the luminosity of the star. This provides values of $L_\star$, $R_\star$, $M_\star$, and an age. With the new ZAMS radii, revised distances are calculated from $D/R_\star$. All objects affected by these ZAMS changes are noted in Table 2. At this point all basic stellar parameters, relevant to this work, have been determined.

4 BALMER EXCESS MEASUREMENTS

With knowledge of the stellar parameters obtained for all targets, a measurement of the Balmer excess, $\Delta D_{\rm B}$, can now be made. $\Delta D_{\rm B}$ is defined as the excess in flux above the intrinsic photospheric flux, seen across the Balmer jump region (this region spans the wavelength range where the hydrogen Balmer series reaches its recombination limit ∼3640–3680 Å). The UV excess is weaker, in terms of energy, in lower mass stars, but is more readily visible due to their cooler photospheres, on top of which the excess can be seen. This UV excess has been measured in both brown dwarfs (Herczeg & Hillenbrand 2008; Herczeg, Cruz & Hillenbrand 2009; Rigliaco et al. 2012) and CTTs (Gullbring et al. 2000; Calvet et al. 2004; Ingleby et al. 2013). From these past studies, the current consensus to the origin of the excess is MA. It has also been shown, in small samples, that an observable $\Delta D_{\rm B}$ in HAeBes stars can be explained within the same context (Muzerolle et al. 2004; Donehew & Brittain 2011; Mendigutía et al. 2011b; Pogodin et al. 2012). We aim to further our understanding of accretion in HAeBes by testing accretion within the context of MA to a large sample of HAeBes; this includes numerous HBes for which little investigation has been done. The Balmer excess is defined as

$$\Delta D_{\rm B} = (U - B)_0 - (U - B)_{\rm dered}, \quad (1)$$

where $(U - B)_0$ is the intrinsic colour of the target and $(U - B)_{\rm dered}$ is the dereddened observed colour index. Detailed below are the two best methods of measurement.

4.1 Method 1 – Spectral matching: single-point measurement

The first approach to measuring $\Delta D_{\rm B}$ uses the spectral region of the UVB arm from 3500 to 4600 Å, and adopts the same techniques employed by Donehew & Brittain (2011). This method requires the spectrum of the target to be compared against the intrinsic spectrum of a star of the same spectral type. The KC-models mentioned earlier are used here as the intrinsic star spectra. Following the calibration in Section 2, the spectrum of each target shows the correct, reddened spectral shape. This allows both the target and model spectra to be normalized to 4000 Å, while preserving their spectral shape. Next,

Table 2. Details of the derived stellar parameters. Stars for which a distance estimate from the literature is used, or if the star was moved to the ZAMS, are noted in the final column (column 10, a legend is provided as a footnote).

Name	$T_{\rm eff}$ (K)	$\log(g)$ (cm s^{-2})	$\log(L_\star)$ ($L_\odot$)	$M_\star$ ($M_\odot$)	$R_\star$ ($R_\odot$)	A_V (mag)	Age (Myr)	Distance (pc)	Notes
UX Ori	8500 ± 250	$3.90^{+0.25}_{-0.25}$	$1.54^{+0.38}_{-0.33}$	$2.1^{+0.7}_{-0.3}$	$2.7^{+0.4}_{-0.2}$	$0.48^{+0.07}_{-0.03}$	$4.24^{+3.24}_{-2.35}$	600^{+96}_{-50}	
PDS 174	17 000 ± 2000	$4.10^{+0.40}_{-0.40}$	$2.91^{+0.56}_{-0.56}$	$5.0^{+2.3}_{-2.3}$	$3.3^{+0.7}_{-0.7}$	$3.51^{+0.07}_{-0.07}$	$0.60^{+0.43}_{-0.43}$	1126^{+238}_{-237}	
V1012 Ori	8500 ± 250	$4.38^{+0.15}_{-0.15}$	$0.94^{+0.28}_{-0.37}$	$1.6^{+0.3}_{-0.3}$	$1.4^{+0.4}_{-0.4}$	$1.32^{+0.02}_{-0.04}$	$15.16^{+7.58}_{-7.58}$	445^{+137}_{-130}	† *
HD 34282	9500 ± 250	$4.40^{+0.15}_{-0.15}$	$1.17^{+0.28}_{-0.36}$	$1.9^{+0.4}_{-0.4}$	$1.4^{+0.4}_{-0.4}$	$0.01^{+0.02}_{-0.00}$	$10.00^{+5.00}_{-5.00}$	366^{+111}_{-109}	
HD 287823	8375 ± 125	$4.23^{+0.11}_{-0.15}$	$1.09^{+0.17}_{-0.20}$	$1.7^{+0.1}_{-0.1}$	$1.7^{+0.3}_{-0.3}$	$0.00^{+0.05}_{-0.00}$	$9.01^{+4.11}_{-2.28}$	340^{+68}_{-68}	† a
HD 287841	7750 ± 250	$4.27^{+0.12}_{-0.12}$	$0.87^{+0.17}_{-0.21}$	$1.5^{+0.1}_{-0.1}$	$1.5^{+0.2}_{-0.2}$	$0.00^{+0.05}_{-0.00}$	$14.07^{+4.10}_{-4.10}$	340^{+68}_{-68}	† a
HD 290409	9750 ± 500	$4.25^{+0.25}_{-0.25}$	$1.42^{+0.29}_{-0.29}$	$2.1^{+0.2}_{-0.2}$	$1.8^{+0.1}_{-0.1}$	$0.00^{+0.05}_{-0.00}$	$5.50^{+2.03}_{-2.03}$	514^{+36}_{-29}	
HD 35929	7000 ± 250	$3.47^{+0.11}_{-0.11}$	$1.76^{+0.17}_{-0.21}$	$2.9^{+0.4}_{-0.4}$	$5.2^{+0.7}_{-0.8}$	$0.00^{+0.05}_{-0.00}$	$1.65^{+0.81}_{-0.55}$	360^{+72}_{-72}	† b
HD 290500	9500 ± 500	$3.80^{+0.40}_{-0.40}$	$1.94^{+0.61}_{-0.53}$	$2.8^{+1.8}_{-0.7}$	$3.5^{+1.0}_{-0.5}$	$0.00^{+0.05}_{-0.00}$	$2.26^{+3.39}_{-1.72}$	1522^{+436}_{-211}	
HD 244314	8500 ± 250	$4.15^{+0.11}_{-0.15}$	$1.21^{+0.18}_{-0.23}$	$1.8^{+0.1}_{-0.1}$	$1.9^{+0.3}_{-0.3}$	$0.10^{+0.02}_{-0.05}$	$7.52^{+1.97}_{-1.96}$	440^{+88}_{-88}	† a
HK Ori	8500 ± 500	$4.22^{+0.13}_{-0.13}$	$1.13^{+0.24}_{-0.27}$	$1.7^{+0.2}_{-0.2}$	$1.7^{+0.3}_{-0.3}$	$1.21^{+0.12}_{-0.14}$	$8.73^{+2.73}_{-2.73}$	440^{+88}_{-88}	† a
HD 244604	9000 ± 250	$3.99^{+0.15}_{-0.13}$	$1.54^{+0.18}_{-0.23}$	$2.1^{+0.3}_{-0.2}$	$2.4^{+0.4}_{-0.5}$	$0.14^{+0.00}_{-0.04}$	$4.56^{+1.53}_{-1.32}$	440^{+88}_{-88}	† a
UY Ori	9750 ± 250	$4.30^{+0.20}_{-0.20}$	$1.36^{+0.23}_{-0.23}$	$2.0^{+0.1}_{-0.1}$	$1.7^{+0.1}_{-0.1}$	$1.11^{+0.02}_{-0.00}$	$6.35^{+1.84}_{-1.84}$	1027^{+38}_{-35}	
HD 245185	10 000 ± 500	$4.25^{+0.25}_{-0.25}$	$1.49^{+0.29}_{-0.29}$	$2.2^{+0.2}_{-0.2}$	$1.8^{+0.1}_{-0.1}$	$0.00^{+0.05}_{-0.00}$	$4.91^{+1.70}_{-1.70}$	519^{+34}_{-28}	
T Ori	9000 ± 500	$3.60^{+0.30}_{-0.30}$	$2.12^{+0.47}_{-0.46}$	$3.3^{+1.5}_{-1.0}$	$4.8^{+1.0}_{-0.8}$	$1.50^{+0.08}_{-0.05}$	$1.35^{+2.27}_{-0.93}$	750^{+159}_{-123}	
V380 Ori	9750 ± 750	$4.00^{+0.35}_{-0.35}$	$1.71^{+0.52}_{-0.26}$	$2.3^{+1.1}_{-0.2}$	$2.5^{+0.5}_{-0.1}$	$2.21^{+0.05}_{-0.07}$	$3.73^{+2.46}_{-2.49}$	330^{+73}_{-17}	
HD 37258	9750 ± 500	$4.25^{+0.25}_{-0.25}$	$1.42^{+0.29}_{-0.29}$	$2.1^{+0.2}_{-0.2}$	$1.8^{+0.1}_{-0.1}$	$0.06^{+0.05}_{-0.04}$	$5.50^{+2.03}_{-2.03}$	424^{+25}_{-22}	
HD 290770	10 500 ± 250	$4.20^{+0.30}_{-0.30}$	$1.64^{+0.38}_{-0.38}$	$2.3^{+0.5}_{-0.5}$	$2.0^{+0.2}_{-0.2}$	$0.00^{+0.05}_{-0.00}$	$4.16^{+1.89}_{-1.89}$	440^{+43}_{-41}	
BF Ori	9000 ± 250	$3.97^{+0.15}_{-0.13}$	$1.57^{+0.19}_{-0.22}$	$2.1^{+0.3}_{-0.2}$	$2.5^{+0.4}_{-0.5}$	$0.33^{+0.03}_{-0.02}$	$4.34^{+1.55}_{-1.32}$	510^{+102}_{-102}	† a
HD 37357	9500 ± 250	$4.10^{+0.10}_{-0.10}$	$1.52^{+0.13}_{-0.11}$	$2.1^{+0.1}_{-0.1}$	$2.1^{+0.1}_{-0.0}$	$0.00^{+0.05}_{-0.00}$	$4.93^{+0.87}_{-0.87}$	344^{+15}_{-4}	
HD 290764	7875 ± 375	$3.90^{+0.17}_{-0.15}$	$1.36^{+0.22}_{-0.26}$	$1.9^{+0.4}_{-0.2}$	$2.6^{+0.5}_{-0.5}$	$0.16^{+0.12}_{-0.14}$	$5.25^{+2.58}_{-1.90}$	470^{+94}_{-94}	† a
HD 37411	9750 ± 250	$4.35^{+0.15}_{-0.15}$	$1.28^{+0.28}_{-0.36}$	$1.9^{+0.4}_{-0.4}$	$1.5^{+0.5}_{-0.5}$	$0.21^{+0.01}_{-0.00}$	$9.00^{+4.50}_{-4.50}$	358^{+109}_{-107}	
V599 Ori	8000 ± 250	$3.72^{+0.13}_{-0.12}$	$1.68^{+0.19}_{-0.23}$	$2.5^{+0.4}_{-0.4}$	$3.6^{+0.6}_{-0.7}$	$4.65^{+0.06}_{-0.07}$	$2.82^{+1.40}_{-1.00}$	510^{+102}_{-102}	† a
V350 Ori	9000 ± 250	$4.18^{+0.11}_{-0.16}$	$1.31^{+0.19}_{-0.22}$	$1.9^{+0.1}_{-0.1}$	$1.9^{+0.3}_{-0.3}$	$0.69^{+0.02}_{-0.03}$	$6.41^{+1.97}_{-1.67}$	510^{+102}_{-102}	† a
HD 250550	11 000 ± 500	$3.80^{+0.40}_{-0.40}$	$2.28^{+0.61}_{-0.53}$	$3.4^{+2.1}_{-0.9}$	$3.8^{+1.0}_{-0.5}$	$0.00^{+0.05}_{-0.00}$	$1.42^{+2.21}_{-1.09}$	973^{+267}_{-136}	
V791 Mon	15 000 ± 1500	$4.30^{+0.16}_{-0.16}$	$2.35^{+0.40}_{-0.51}$	$3.6^{+0.7}_{-0.7}$	$2.2^{+0.7}_{-0.7}$	$1.17^{+0.06}_{-0.04}$	$1.80^{+0.90}_{-0.90}$	648^{+204}_{-184}	
PDS 124	10 250 ± 250	$4.30^{+0.20}_{-0.20}$	$1.47^{+0.23}_{-0.23}$	$2.2^{+0.2}_{-0.2}$	$1.7^{+0.1}_{-0.1}$	$1.23^{+0.03}_{-0.00}$	$5.48^{+1.64}_{-1.64}$	894^{+34}_{-33}	
LkHa 339	10 500 ± 250	$4.20^{+0.20}_{-0.20}$	$1.64^{+0.24}_{-0.24}$	$2.3^{+0.2}_{-0.2}$	$2.0^{+0.1}_{-0.1}$	$3.54^{+0.01}_{-0.01}$	$4.16^{+1.18}_{-1.18}$	597^{+27}_{-25}	
VY Mon	12 000 ± 4000	$3.75^{+0.50}_{-0.50}$	$2.56^{+0.77}_{-0.65}$	$4.0^{+3.7}_{-1.3}$	$4.4^{+1.6}_{-0.7}$	$5.68^{+0.17}_{-0.45}$	$0.89^{+2.61}_{-0.80}$	439^{+181}_{-113}	
R Mon	12 000 ± 2000	$4.00^{+0.11}_{-0.24}$	$2.19^{+0.34}_{-0.40}$	$3.1^{+0.8}_{-0.6}$	$2.9^{+0.3}_{-0.3}$	$2.42^{+0.08}_{-0.13}$	$1.92^{+1.23}_{-0.89}$	800^{+160}_{-160}	† c
V590 Mon	12 500 ± 1000	$4.20^{+0.30}_{-0.30}$	$2.06^{+0.37}_{-0.37}$	$3.1^{+0.6}_{-0.6}$	$2.3^{+0.2}_{-0.2}$	$1.03^{+0.04}_{-0.05}$	$2.19^{+1.00}_{-1.00}$	1722^{+171}_{-160}	
PDS 24	10 500 ± 500	$4.20^{+0.30}_{-0.30}$	$1.64^{+0.38}_{-0.38}$	$2.3^{+0.5}_{-0.5}$	$2.0^{+0.2}_{-0.2}$	$1.11^{+0.04}_{-0.03}$	$4.16^{+1.91}_{-1.91}$	1646^{+162}_{-157}	
PDS 130	10 500 ± 250	$3.90^{+0.20}_{-0.20}$	$2.02^{+0.30}_{-0.27}$	$2.8^{+0.7}_{-0.4}$	$3.1^{+0.4}_{-0.2}$	$2.07^{+0.01}_{-0.00}$	$2.25^{+1.32}_{-1.07}$	1748^{+216}_{-129}	
PDS 229N	12 500 ± 250	$4.20^{+0.20}_{-0.20}$	$2.06^{+0.23}_{-0.23}$	$3.1^{+0.2}_{-0.2}$	$2.3^{+0.1}_{-0.1}$	$2.03^{+0.01}_{-0.01}$	$2.19^{+0.63}_{-0.63}$	1379^{+57}_{-56}	
GU CMa	22 500 ± 1500	$3.90^{+0.40}_{-0.40}$	$3.87^{+0.62}_{-0.62}$	$9.5^{+6.8}_{-6.8}$	$5.7^{+1.7}_{-1.7}$	$0.57^{+0.03}_{-0.02}$	$0.11^{+0.10}_{-0.10}$	531^{+163}_{-163}	
HT CMa	10 500 ± 500	$4.00^{+0.20}_{-0.20}$	$1.88^{+0.29}_{-0.24}$	$2.6^{+0.6}_{-0.2}$	$2.6^{+0.3}_{-0.1}$	$0.23^{+0.05}_{-0.02}$	$2.96^{+1.19}_{-1.32}$	1634^{+187}_{-72}	
Z CMa	8500 ± 500	$2.53^{+0.17}_{-0.17}$	$3.62^{+0.24}_{-0.28}$	$11.0^{+1.7}_{-1.7}$	$29.8^{+5.2}_{-5.3}$	$3.37^{+0.12}_{-0.16}$	$0.03^{+0.02}_{-0.02}$	1050^{+210}_{-210}	† d
HU CMa	13 000 ± 250	$4.20^{+0.20}_{-0.20}$	$2.16^{+0.23}_{-0.23}$	$3.2^{+0.2}_{-0.2}$	$2.4^{+0.1}_{-0.1}$	$0.80^{+0.02}_{-0.01}$	$1.88^{+0.52}_{-0.52}$	1240^{+47}_{-46}	
HD 53367	29 500 ± 1000	$4.25^{+0.25}_{-0.25}$	$4.11^{+0.37}_{-0.37}$	$12.3^{+4.2}_{-4.2}$	$4.3^{+0.7}_{-0.7}$	$1.88^{+0.02}_{-0.01}$	$0.08^{+0.08}_{-0.08}$	340^{+53}_{-54}	
PDS 241	26 000 ± 1500	$4.00^{+0.30}_{-0.30}$	$4.11^{+0.46}_{-0.46}$	$11.6^{+5.5}_{-5.5}$	$5.6^{+1.2}_{-1.2}$	$2.60^{+0.04}_{-0.01}$	$0.08^{+0.07}_{-0.07}$	2907^{+614}_{-617}	
NX Pup	7000 ± 250	$3.78^{+0.13}_{-0.13}$	$1.28^{+0.20}_{-0.21}$	$1.9^{+0.3}_{-0.3}$	$3.0^{+0.5}_{-0.5}$	$0.00^{+0.07}_{-0.00}$	$4.92^{+2.37}_{-1.67}$	410^{+82}_{-82}	† a
PDS 27	17 500 ± 3500	$3.16^{+0.27}_{-0.27}$	$4.39^{+0.40}_{-0.40}$	$15.3^{+5.4}_{-4.4}$	$17.0^{+4.0}_{-4.0}$	$5.03^{+0.13}_{-0.13}$	$0.10^{+0.10}_{-0.10}$	3170^{+660}_{-620}	† e
PDS 133	14 000 ± 2000	$4.08^{+0.12}_{-0.11}$	$2.46^{+0.33}_{-0.38}$	$3.7^{+0.9}_{-0.7}$	$2.9^{+0.4}_{-0.4}$	$1.43^{+0.09}_{-0.10}$	$1.27^{+0.94}_{-0.56}$	2500^{+500}_{-500}	† f
HD 59319	12 500 ± 500	$3.50^{+0.20}_{-0.20}$	$3.03^{+0.31}_{-0.30}$	$5.7^{+1.6}_{-1.2}$	$7.0^{+0.9}_{-0.8}$	$0.00^{+0.05}_{-0.00}$	$0.32^{+0.34}_{-0.17}$	1218^{+162}_{-137}	
PDS 134	14 000 ± 500	$3.40^{+0.30}_{-0.30}$	$3.45^{+0.46}_{-0.45}$	$7.6^{+3.5}_{-2.3}$	$9.1^{+1.9}_{-1.5}$	$1.22^{+0.03}_{-0.02}$	$0.15^{+0.28}_{-0.10}$	5687^{+1178}_{-931}	
HD 68695	9250 ± 250	$4.40^{+0.15}_{-0.15}$	$1.11^{+0.28}_{-0.37}$	$1.8^{+0.4}_{-0.4}$	$1.4^{+0.4}_{-0.4}$	$0.00^{+0.05}_{-0.00}$	$10.00^{+5.00}_{-5.00}$	344^{+106}_{-103}	
HD 72106	8750 ± 250	$3.89^{+0.13}_{-0.12}$	$1.63^{+0.18}_{-0.21}$	$2.3^{+0.3}_{-0.3}$	$2.8^{+0.5}_{-0.5}$	$0.00^{+0.05}_{-0.00}$	$3.76^{+1.47}_{-1.18}$	370^{+74}_{-74}	† a

Table 2 – *continued.*

Name	$T_{\rm eff}$ (K)	$\log(g)$ (cm s^{-2}]	$\log(L_\star)$ ($L_\odot$)	$M_\star$ ($M_\odot$)	$R_\star$ ($R_\odot$)	A_V (mag)	Age (Myr)	Distance (pc)	Notes
TYC 8581-2002-1	9750 ± 250	$4.00^{+0.10}_{-0.10}$	$1.71^{+0.14}_{-0.12}$	$2.3^{+0.2}_{-0.1}$	$2.5^{+0.1}_{-0.1}$	$0.94^{+0.04}_{-0.00}$	$3.73^{+0.78}_{-0.89}$	902^{+47}_{-25}	
PDS 33	9750 ± 250	$4.40^{+0.15}_{-0.15}$	$1.23^{+0.27}_{-0.36}$	$1.9^{+0.4}_{-0.4}$	$1.4^{+0.4}_{-0.4}$	$0.52^{+0.04}_{-0.00}$	$9.00^{+4.50}_{-4.50}$	932^{+282}_{-279}	*
HD 76534	19 000 ± 500	$4.10^{+0.20}_{-0.20}$	$3.18^{+0.26}_{-0.20}$	$6.0^{+0.9}_{-0.6}$	$3.6^{+0.3}_{-0.2}$	$0.62^{+0.02}_{-0.01}$	$0.37^{+0.19}_{-0.14}$	568^{+43}_{-29}	
PDS 281	16 000 ± 1500	$3.50^{+0.30}_{-0.30}$	$3.62^{+0.47}_{-0.45}$	$8.3^{+4.0}_{-2.5}$	$8.5^{+1.8}_{-1.4}$	$1.89^{+0.07}_{-0.10}$	$0.12^{+0.23}_{-0.09}$	936^{+207}_{-168}	
PDS 286	30 000 ± 3000	$4.25^{+0.16}_{-0.16}$	$4.18^{+0.41}_{-0.52}$	$13.5^{+2.7}_{-2.7}$	$4.6^{+1.5}_{-1.5}$	$6.27^{+0.05}_{-0.04}$	$0.10^{+0.05}_{-0.05}$	521^{+167}_{-146}	
PDS 297	10 750 ± 250	$4.00^{+0.20}_{-0.20}$	$1.93^{+0.29}_{-0.24}$	$2.6^{+0.6}_{-0.2}$	$2.7^{+0.3}_{-0.1}$	$0.81^{+0.01}_{-0.02}$	$2.77^{+1.12}_{-1.22}$	1465^{+166}_{-59}	
HD 85567	13 000 ± 500	$3.50^{+0.30}_{-0.30}$	$3.13^{+0.46}_{-0.45}$	$6.0^{+2.7}_{-1.8}$	$7.2^{+1.5}_{-1.2}$	$0.89^{+0.03}_{-0.02}$	$0.27^{+0.52}_{-0.18}$	907^{+183}_{-146}	
HD 87403	10 000 ± 250	$3.30^{+0.10}_{-0.10}$	$2.83^{+0.15}_{-0.15}$	$5.5^{+0.7}_{-0.6}$	$8.7^{+0.6}_{-0.5}$	$0.00^{+0.05}_{-0.00}$	$0.32^{+0.15}_{-0.10}$	1801^{+125}_{-109}	
PDS 37	17 500 ± 3500	$2.94^{+0.35}_{-0.35}$	$4.75^{+0.39}_{-0.39}$	$21.1^{+11.0}_{-5.3}$	$25.8^{+5.0}_{-5.0}$	$5.81^{+0.13}_{-0.13}$	$0.10^{+0.10}_{-0.10}$	4310^{+670}_{-670}	† e
HD 305298	34 000 ± 1000	$4.31^{+0.16}_{-0.16}$	$4.46^{+0.23}_{-0.41}$	$15.7^{+3.1}_{-3.1}$	$4.6^{+1.4}_{-1.4}$	$1.30^{+0.00}_{-0.02}$	$0.02^{+0.01}_{-0.01}$	3366^{+1010}_{-979}	*
HD 94509	11 500 ± 1000	$2.90^{+0.40}_{-0.40}$	$3.76^{+0.65}_{-0.62}$	$10.8^{+9.0}_{-4.3}$	$19.2^{+6.8}_{-4.3}$	$0.00^{+0.05}_{-0.00}$	$0.05^{+0.16}_{-0.05}$	4384^{+1585}_{-1009}	
HD 95881	10 000 ± 250	$3.20^{+0.10}_{-0.10}$	$2.98^{+0.15}_{-0.15}$	$6.2^{+0.8}_{-0.7}$	$10.3^{+0.7}_{-0.6}$	$0.00^{+0.05}_{-0.00}$	$0.21^{+0.10}_{-0.07}$	1290^{+90}_{-78}	
HD 96042	25 500 ± 1500	$3.80^{+0.20}_{-0.20}$	$4.36^{+0.33}_{-0.29}$	$14.0^{+5.1}_{-2.8}$	$7.8^{+1.3}_{-0.8}$	$0.78^{+0.03}_{-0.01}$	$0.02^{+0.05}_{-0.02}$	1792^{+302}_{-197}	
HD 97048	10 500 ± 500	$4.30^{+0.20}_{-0.20}$	$1.52^{+0.23}_{-0.23}$	$2.2^{+0.2}_{-0.2}$	$1.7^{+0.1}_{-0.1}$	$0.90^{+0.05}_{-0.02}$	$5.12^{+1.52}_{-1.52}$	171^{+7}_{-7}	
HD 98922	10 500 ± 250	$3.60^{+0.10}_{-0.10}$	$2.48^{+0.15}_{-0.15}$	$4.0^{+0.5}_{-0.5}$	$5.2^{+0.3}_{-0.3}$	$0.09^{+0.01}_{-0.00}$	$0.84^{+0.35}_{-0.26}$	346^{+22}_{-20}	
HD 100453	7250 ± 250	$4.08^{+0.15}_{-0.13}$	$0.93^{+0.17}_{-0.21}$	$1.5^{+0.2}_{-0.1}$	$1.9^{+0.3}_{-0.3}$	$0.00^{+0.05}_{-0.00}$	$9.97^{+6.29}_{-2.79}$	122^{+24}_{-25}	† b
HD 100546	9750 ± 500	$4.34^{+0.06}_{-0.06}$	$1.29^{+0.14}_{-0.14}$	$1.9^{+0.1}_{-0.1}$	$1.5^{+0.1}_{-0.1}$	$0.00^{+0.05}_{-0.00}$	$7.02^{+1.49}_{-1.49}$	97^{+10}_{-10}	† b
HD 101412	9750 ± 250	$4.30^{+0.20}_{-0.20}$	$1.36^{+0.23}_{-0.23}$	$2.0^{+0.1}_{-0.1}$	$1.7^{+0.1}_{-0.1}$	$0.21^{+0.03}_{-0.00}$	$6.35^{+1.84}_{-1.84}$	301^{+11}_{-10}	
PDS 344	15 250 ± 500	$4.30^{+0.20}_{-0.20}$	$2.39^{+0.25}_{-0.25}$	$3.7^{+0.5}_{-0.5}$	$2.3^{+0.1}_{-0.1}$	$0.86^{+0.01}_{-0.02}$	$1.48^{+0.52}_{-0.52}$	2756^{+172}_{-165}	
HD 104237	8000 ± 250	$3.89^{+0.12}_{-0.12}$	$1.41^{+0.17}_{-0.21}$	$2.0^{+0.3}_{-0.2}$	$2.6^{+0.4}_{-0.4}$	$0.00^{+0.05}_{-0.00}$	$4.92^{+1.87}_{-1.46}$	115^{+23}_{-23}	† b
V1028 Cen	14 000 ± 500	$3.80^{+0.30}_{-0.30}$	$2.85^{+0.45}_{-0.41}$	$4.7^{+2.0}_{-1.0}$	$4.5^{+0.9}_{-0.5}$	$0.57^{+0.01}_{-0.03}$	$0.59^{+0.69}_{-0.39}$	1843^{+355}_{-215}	
PDS 361S	18 500 ± 1000	$3.80^{+0.30}_{-0.30}$	$3.53^{+0.46}_{-0.41}$	$7.4^{+3.2}_{-1.7}$	$5.7^{+1.1}_{-0.7}$	$1.90^{+0.04}_{-0.01}$	$0.19^{+0.23}_{-0.12}$	4385^{+872}_{-541}	
HD 114981	16 000 ± 500	$3.60^{+0.20}_{-0.20}$	$3.47^{+0.30}_{-0.30}$	$7.3^{+2.0}_{-1.5}$	$7.1^{+0.9}_{-0.8}$	$0.00^{+0.05}_{-0.00}$	$0.18^{+0.17}_{-0.09}$	908^{+118}_{-99}	
PDS 364	12 500 ± 1000	$4.20^{+0.20}_{-0.20}$	$2.06^{+0.23}_{-0.23}$	$3.1^{+0.2}_{-0.2}$	$2.3^{+0.1}_{-0.1}$	$1.87^{+0.05}_{-0.03}$	$2.19^{+0.58}_{-0.58}$	1715^{+97}_{-91}	
PDS 69	15 000 ± 2000	$4.00^{+0.35}_{-0.35}$	$2.72^{+0.52}_{-0.76}$	$4.3^{+2.0}_{-1.5}$	$3.4^{+0.7}_{-0.6}$	$1.60^{+0.07}_{-0.07}$	$0.84^{+2.02}_{-0.62}$	630^{+141}_{-126}	
DG Cir	11 000 ± 3000	$4.41^{+0.18}_{-0.18}$	$1.49^{+0.68}_{-0.93}$	$2.2^{+0.4}_{-0.4}$	$1.5^{+0.5}_{-0.5}$	$3.94^{+0.13}_{-0.54}$	$5.95^{+2.97}_{-2.97}$	713^{+250}_{-184}	† *
HD 132947	10 250 ± 250	$3.90^{+0.10}_{-0.10}$	$1.97^{+0.15}_{-0.14}$	$2.7^{+0.3}_{-0.3}$	$3.1^{+0.2}_{-0.1}$	$0.00^{+0.05}_{-0.00}$	$2.44^{+0.77}_{-0.65}$	565^{+35}_{-26}	
HD 135344B	6375 ± 125	$3.94^{+0.12}_{-0.12}$	$0.85^{+0.18}_{-0.22}$	$1.5^{+0.2}_{-0.2}$	$2.2^{+0.4}_{-0.4}$	$0.23^{+0.05}_{-0.06}$	$7.99^{+3.24}_{-2.34}$	140^{+28}_{-28}	† a
HD 139614	7750 ± 250	$4.31^{+0.12}_{-0.12}$	$0.82^{+0.17}_{-0.21}$	$1.5^{+0.1}_{-0.1}$	$1.4^{+0.2}_{-0.2}$	$0.00^{+0.05}_{-0.00}$	$15.64^{+4.29}_{-4.29}$	140^{+28}_{-28}	† a
PDS 144S	7750 ± 250	$4.13^{+0.14}_{-0.16}$	$1.02^{+0.20}_{-0.23}$	$1.6^{+0.2}_{-0.1}$	$1.8^{+0.3}_{-0.3}$	$0.57^{+0.07}_{-0.08}$	$9.45^{+4.81}_{-2.88}$	1000^{+200}_{-200}	† f
HD 141569	9750 ± 250	$4.35^{+0.15}_{-0.15}$	$1.28^{+0.28}_{-0.37}$	$1.9^{+0.4}_{-0.4}$	$1.5^{+0.5}_{-0.5}$	$0.01^{+0.01}_{-0.00}$	$9.00^{+4.50}_{-4.50}$	112^{+34}_{-33}	
HD 141926	28 000 ± 1500	$3.75^{+0.25}_{-0.25}$	$4.70^{+0.26}_{-0.37}$	$19.4^{+4.5}_{-5.0}$	$9.7^{+1.1}_{-1.3}$	$2.40^{+0.03}_{-0.04}$	$0.00^{+0.03}_{-0.00}$	1254^{+143}_{-175}	
HD 142666	7500 ± 250	$4.13^{+0.11}_{-0.16}$	$0.96^{+0.20}_{-0.24}$	$1.6^{+0.2}_{-0.1}$	$1.8^{+0.3}_{-0.3}$	$0.50^{+0.08}_{-0.09}$	$10.43^{+6.21}_{-3.34}$	145^{+29}_{-29}	† a
HD 142527	6500 ± 250	$3.93^{+0.08}_{-0.08}$	$0.90^{+0.12}_{-0.13}$	$1.6^{+0.1}_{-0.1}$	$2.2^{+0.1}_{-0.2}$	$0.00^{+0.05}_{-0.00}$	$8.08^{+1.94}_{-1.63}$	140^{+20}_{-20}	† g
HD 144432	7500 ± 250	$4.05^{+0.17}_{-0.14}$	$1.04^{+0.19}_{-0.21}$	$1.6^{+0.2}_{-0.1}$	$2.0^{+0.3}_{-0.3}$	$0.00^{+0.06}_{-0.00}$	$8.72^{+4.81}_{-2.50}$	160^{+32}_{-32}	† b
HD 144668	8500 ± 250	$3.75^{+0.13}_{-0.12}$	$1.76^{+0.19}_{-0.22}$	$2.5^{+0.4}_{-0.4}$	$3.5^{+0.6}_{-0.6}$	$0.33^{+0.05}_{-0.04}$	$2.70^{+1.32}_{-0.93}$	160^{+32}_{-32}	† b
HD 145718	8000 ± 250	$4.37^{+0.15}_{-0.15}$	$0.82^{+0.29}_{-0.37}$	$1.5^{+0.3}_{-0.3}$	$1.3^{+0.4}_{-0.4}$	$0.74^{+0.06}_{-0.05}$	$19.54^{+9.77}_{-9.77}$	134^{+41}_{-39}	† *
PDS 415N	6250 ± 250	$4.47^{+0.15}_{-0.15}$	$0.13^{+0.30}_{-0.39}$	$1.1^{+0.2}_{-0.2}$	$1.0^{+0.3}_{-0.3}$	$1.11^{+0.11}_{-0.15}$	$336.02^{+168.01}_{-168.01}$	197^{+60}_{-58}	† *
HD 150193	9000 ± 250	$4.27^{+0.17}_{-0.17}$	$1.21^{+0.19}_{-0.23}$	$1.9^{+0.1}_{-0.1}$	$1.7^{+0.3}_{-0.3}$	$1.55^{+0.02}_{-0.04}$	$7.22^{+1.89}_{-1.89}$	120^{+24}_{-24}	† h
AK Sco	6250 ± 250	$4.26^{+0.10}_{-0.10}$	$0.38^{+0.18}_{-0.20}$	$1.2^{+0.1}_{-0.1}$	$1.3^{+0.2}_{-0.2}$	$0.00^{+0.05}_{-0.00}$	$17.71^{+4.71}_{-3.42}$	103^{+20}_{-21}	† b
PDS 431	10 500 ± 500	$3.70^{+0.20}_{-0.20}$	$2.32^{+0.31}_{-0.30}$	$3.5^{+1.0}_{-0.7}$	$4.4^{+0.6}_{-0.5}$	$1.76^{+0.03}_{-0.03}$	$1.19^{+1.07}_{-0.61}$	2875^{+384}_{-316}	
KK Oph	8500 ± 500	$4.38^{+0.15}_{-0.15}$	$0.94^{+0.33}_{-0.43}$	$1.6^{+0.3}_{-0.3}$	$1.4^{+0.4}_{-0.4}$	$2.70^{+0.10}_{-0.15}$	$15.16^{+7.58}_{-7.58}$	279^{+86}_{-81}	† *
HD 163296	9250 ± 250	$4.30^{+0.20}_{-0.20}$	$1.23^{+0.23}_{-0.23}$	$1.9^{+0.1}_{-0.1}$	$1.6^{+0.0}_{-0.0}$	$0.00^{+0.05}_{-0.00}$	$7.56^{+2.17}_{-2.17}$	101^{+4}_{-3}	
MWC 297	24 500 ± 1500	$4.00^{+0.30}_{-0.30}$	$3.95^{+0.46}_{-0.46}$	$10.2^{+4.6}_{-4.6}$	$5.3^{+1.1}_{-1.1}$	$8.47^{+0.04}_{-0.03}$	$0.10^{+0.08}_{-0.08}$	170^{+34}_{-34}	

†A literature distance is initially adopted to these stars, as $\log(g)$ cannot be determined from the spectra alone. *Stars which have been placed on the ZAMS. References: (a) de Zeeuw et al. (1999), (b) van Leeuwen (2007), (c) Dahm & Simon (2005), (d) Shevchenko et al. (1999), (e) Ababakr et al. (2015), (f) Vieira et al. (2003), (g) Fukagawa et al. (2006), (h) Loinard et al. (2008).

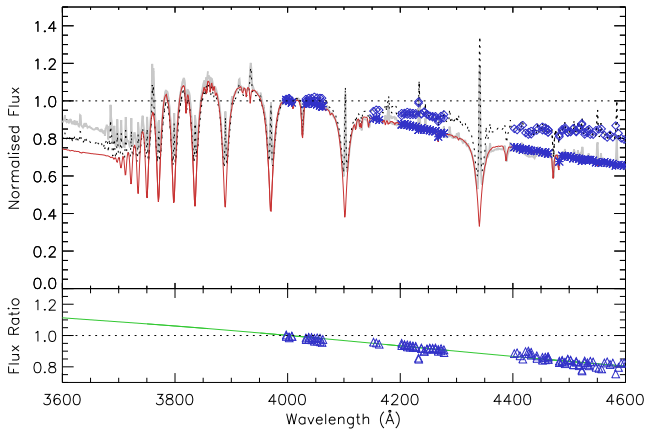

Figure 5. An example of the method 1 technique of measuring $\Delta D_{\rm B}$ is shown here. Initially, the observed spectrum (dashed black) and the intrinsic spectrum (red, a KC-model matching the spectral type of the target) have been normalized to 4000 Å. Continuum points are selected from these between 4000 and 4600 Å (shown as blue points). A ratio of these is provided in the bottom panel and they are fitted by a reddening law, which is extrapolated to 3600 Å. This level of reddening correction is then applied to the original spectrum, with the result plotted in the top panel (grey). The SED of the model and the corrected spectra are now exactly the same between 4000 and 4600 Å, allowing measurement of the Balmer excess to be performed using only the region around 3600 Å.

a correction for reddening present in the observed spectra is performed. To do this, the difference between the measured continuum of the target and the model within 4000–4600 Å is fitted by a reddening law [the reddening law of Cardelli et al. (1989) is used here]. This also provides a best-fitting A_V. Extinction correction is applied to the whole spectrum, while maintaining the 4000 Å pivot point for this correction. The result of this method is that the spectral shape of the target is adjusted such that the slope between the intrinsic model and the target spectrum now matches. The success of this normalization is independent of the amount of extinction towards the star (Muzerolle et al. 2004; Donehew & Brittain 2011). Fig. 5 shows the application of this spectral slope matching technique along with an example output.

To perform the measurement of $\Delta D_{\rm B}$, attention must be drawn back to equation (1), where the magnitudes are now converted into a flux:

$$\Delta D_{\rm B} = -2.5 \log \left(\frac{F_U^{\rm phot}}{F_B^{\rm phot}} \right) + 2.5 \log \left(\frac{F_U^{\rm dered}}{F_B^{\rm dered}} \right), \quad (2)$$

where F is the flux, with subscripts denoting the corresponding wavelength region, and the superscripts are: the intrinsic flux denoted by 'phot' and the dereddened flux denoted by 'dered'. For these measurements, the fluxes are monochromatic. Now, consider the fact that the observed, dereddened flux includes an accretion contribution, such that $F_U^{\rm dered} = F_U^{\rm phot} + F_U^{\rm acc}$. This allows the above equation to be written as

$$\Delta D_{\rm B} = 2.5 \log \left(\frac{F_U^{\rm phot} + F_U^{\rm acc}}{F_B^{\rm phot} + F_B^{\rm acc}} \times \frac{F_B^{\rm phot}}{F_U^{\rm phot}} \right). \quad (3)$$

This equation can be reduced through the use of a normalization factor $\alpha^{\rm norm}$, where $(F_B^{\rm phot} + F_B^{\rm acc}) \times \alpha^{\rm norm} = F_B^{\rm phot}$. This normalization across the B band is performed automatically by matching the slope of the spectrum of the target to the intrinsic spectrum's slope (see the steps mentioned earlier). In essence, $\alpha^{\rm norm}$ represents a reddening law. This gives us the final form of the $\Delta D_{\rm B}$ equation:

$$\Delta D_{\rm B} = 2.5 \log \left(\frac{F_U^{\rm phot,norm} + F_U^{\rm acc,norm}}{F_U^{\rm phot}} \right). \quad (4)$$

By these definitions, the $F_U^{\rm phot,norm} + F_U^{\rm acc,norm}$ is just the flux observed from the target spectra and $F_U^{\rm phot}$ can be taken from a KC-model of the same spectral type. Since the spectrum obtained is of medium resolution, we adopt a narrow, monochromatic, range over a typical broad-band filter to represent the U-band magnitude. This also gives us better precision in measurements. The wavelength region of measurement is 3500–3680 Å. This is chosen as it is beyond the Balmer recombination limit. However, two of the echelle orders of X-shooter overlap in this region, and the SNR in an echelle order decreases as wavelength decreases. Therefore, to minimize errors, the 3500–3600 Å region from echelle order 21 and the 3600–3680 Å region from echelle order 20 are measured and combined to give the most accurate result.

4.2 Method 2 – *B*-band normalized, multi-point measurements

An alternate method of measuring $\Delta D_{\rm B}$ is given by Mendigutía et al. (2013), which also does not require the reddening towards a star to be known. This method covers a larger wavelength range, requiring measurements of both the U-band and V-band points. These two points are measured from the observed spectra and a KC-model of the same spectral type (the same model as in method 1), after normalization to the B band. Rather than correcting for A_V, as in the previous method, reddening independence is achieved by expanding equation (1) and substituting in an expression for each reddening component: $A_\lambda = A_V(k_\lambda/k_V)$, where A_λ and A_V are the extinction at any given wavelength and in the V band, respectively. Similarly, k_λ and k_V are the opacities for any given wavelength and the V band, respectively. Applying the expression for A_V to equation (1) gives

$$\Delta D_{\rm B} = (U-B)^{\rm int} - (U-B)^{\rm obs} + A_V \left(\frac{k_U}{k_V} - \frac{k_B}{k_V} \right). \quad (5)$$

The superscript 'int' refers to the intrinsic magnitudes (from a KC-model in this case), while the superscript 'obs' refers to the observed magnitudes (from the observed spectra). The values of the opacities are determined by the reddening law adopted. The reddening law of Cardelli et al. (1989) is used here with an $R_V = 3.1$, providing $k_U/k_V = 1.57$ and $k_B/k_V = 1.33$. To remove the A_V term, the relationship between A_V and colour excess needs to be used: $A_V = {\rm R}_V E(B-V)$. At this point, it should be noted that the method is now reddening independent, since A_V has been removed, but remains dependent on the reddening law adopted, as this affects the opacity ratios. This new form for the Balmer excess is

$$\Delta D_{\rm B} = (U-B)^{\rm int} - (U-B)^{\rm obs} + {\rm R}_V \left(\frac{k_U}{k_V} - \frac{k_B}{k_V} \right) [(B-V)^{\rm obs} - (B-V)^{\rm int}] \quad (6)$$

which can be expressed in terms of flux, instead of magnitudes, as follows:

$$\Delta D_{\rm B} = 2.5 \log \left(\frac{F_U^{\rm obs} \alpha^{\rm norm} F_B^{\rm phot}}{F_B^{\rm obs} \alpha^{\rm norm} F_U^{\rm phot}} \right) + 2.5\, {\rm R}_V \left(\frac{k_U}{k_V} - \frac{k_B}{k_V} \right) \log \left(\frac{F_V^{\rm obs} \alpha^{\rm norm} F_B^{\rm phot}}{F_B^{\rm obs} \alpha^{\rm norm} F_V^{\rm phot}} \right), \quad (7)$$

where $\alpha^{\rm norm}$ has been added and is a normalizing factor for the B band, as seen in method 1, but the normalization is instead performed such that the spectra will be unity at 4400 Å. Note that all these fluxes are considered monochromatic, with centres at the usual Johnson *UBV* wavelengths. This normalization allows the equation to reduce to its final form:

$$\Delta D_{\rm B} = 2.5 \log \left(\frac{F_U^{\rm obs,norm}}{F_U^{\rm phot}} \right) + 2.5\, {\rm R}_V \left(\frac{k_U}{k_V} - \frac{k_B}{k_V} \right) \log \left(\frac{F_V^{\rm obs,norm}}{F_V^{\rm phot}} \right); \quad (8)$$

in this form it can be seen that only four points need to be measured in order to obtain $\Delta D_{\rm B}$ (two from the target spectra, two from the model).

4.3 Comparisons and checks

The two methods used are similar but have some subtle differences. One is that the central wavelength for the B-band normalization is different between the two; it is centred at 4000 Å for method 1, and is centred at 4400 Å for method 2. The next difference is that method 1 performs a reddening correction using a section of the observed spectrum and relies on matching this to a stellar model. On the other hand, method 2 avoids having to make a reddening correction by incorporating the adopted reddening law into the equation for $\Delta D_{\rm B}$, and applies this over a much larger spectral region. Also, both approaches have been adapted from a definition which was based on broad-band photometry. Therefore, some checks need to be made to see whether both approaches are comparable to each other.

The first check is between how the A_V values determined in Section 3 compare with the A_V values extracted from method 1, as the fitting between 4000 and 4600 Å can be used to infer an A_V value. Fig. 6 displays this comparison. In this figure, the standard deviation between the two is found to be 0.60 mag, and is represented by the dashed black lines. Within this 1σ interval, 79 per cent of the sample are included. This helps to highlight that the majority of the sample are tightly correlated, while the outliers are more extreme and actually skew the standard deviation towards them. There are seven stars showing differences greater than 2σ from the mean. One of these is VY Mon which has the lowest SNR of the objects in the blue because it is very extinct. This makes the spectral shape adjustment more difficult and less accurate than other targets. The other outliers often have large A_V and/or large $\Delta D_{\rm B}$ values. This is not entirely unexpected as a significant excess can affect the SED shape of the spectra, which would complicate both photometry fitting and the spectral shape adjustments performed. In general, for HAeBes this is less likely as they are already very hot and the excesses need to be very strong to significantly affect the SED. One source of discrepancy lies in how the photometric method is coarse but covers the *BVRI* points, while the spectral method covers a very narrow wavelength range of 4000–4600 Å, but with a greater accuracy in that region. The photometry used is also not simultaneous with the spectra; variability could therefore also play a role in the differences. Ultimately, this scatter is quite low with few outliers; this is more than acceptable considering the above factors and the standard reddening law adopted in both cases.

The next check is to see how $\Delta D_{\rm B}$ varies between the two methods of measurement; Fig. 7 shows the comparison. There is a systematic offset of ∼0.02 towards method 2 producing higher values, while the standard deviation of scatter between the two methods is ∼0.04 mag. These differences are less than the systematic

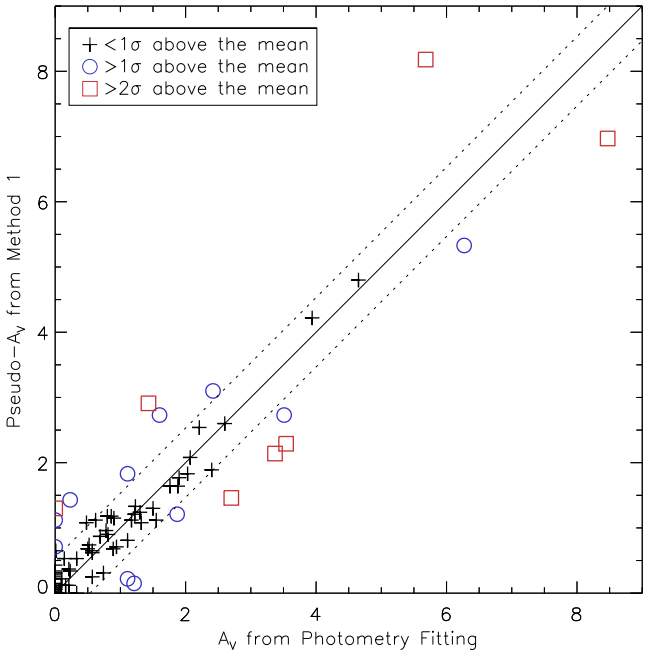

Figure 6. A comparison of a pseudo-A_V, extracted from the method 1 measurement of $\Delta D_{\rm B}$ depending upon how much the spectra were adjusted, against the A_V determined from the photometry fitting in Section 3.2. The solid black line is the line of correlation, while the dashed lines are 1σ deviations, of 0.60 mag from this. Only 8 per cent of the targets are outside 2σ; these often have the largest A_V values (these will be discussed in the text). Errors in the photometric A_V are typically 0.05–0.15 (about the width of the points), and are given in Table 2.

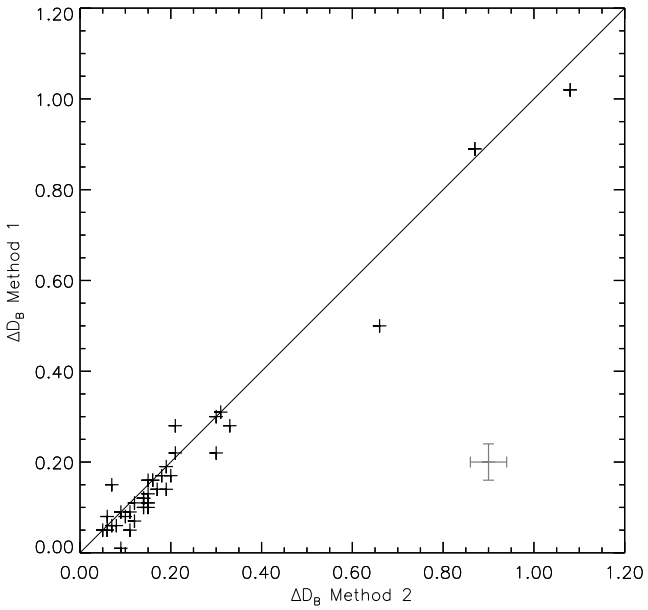

Figure 7. A comparison is made between the two different methods of measuring $\Delta D_{\rm B}$ (detailed in Sections 4.1 and 4.2). A line of expected 1:1 correlation is shown in black. For clarity, individual error bars are not plotted due to the tightness of the points. Instead, a typical error bar of 0.04 mag is plotted in the bottom-right corner. The actual errors range between 0.04 and 0.10 mag, and are provided in Table 3.

error on measurements. Since the original $\Delta D_{\rm B}$ equation, equation (1), can be seen to contain a dereddened term, the differences can be mostly attributed to how the reddening corrections are made in each case, though the normalization of the spectra and points of measurement also influence the result. Method 1 covers a small wavelength range of 3600–4600 Å, of which only the 4000–4600 Å region is used for the reddening correction. This means that this approach is not particularly sensitive to a given reddening law due to the small wavelength range it covers, and can be deemed reddening independent for low levels of extinction ($A_V < 10$). On the other hand, method 2 depends more upon the adopted reddening law than method 1, because it covers a larger wavelength region of 3600–5500 Å. Depending on the R_V selected, the resulting opacity ratios, seen in equation (6), can change substantially, which in turn alters the measured $\Delta D_{\rm B}$. Changing R_V in method 1 does not noticeably affect $\Delta D_{\rm B}$, for low A_V values, as it is always the spectral profiles which are being matched. Through this matching the A_V used will change to retain the SED shape and keeps $\Delta D_{\rm B}$ the same. Returning to the figure, a few outliers can be seen between the two methods; the majority of these are objects with high extinction, or which were identified as having a discrepant A_V between the photometric method and the spectral method in which they were determined.

Overall, consistency is apparent between the methods employed here as the majority of measurements from each method lie within the errors of each other (see Table 3). Based on the above analysis, we deem the methods equivalent. Therefore, in each case an average of the two will be taken for the final result; if one method has a lower measurement error, then that method will be favoured over the other (this can occur depending on emission lines in both the measurement and normalization regions). The $\Delta D_{\rm B}$ value for each star, along with the errors and method(s) used to obtain it, is detailed in Table 3. The errors given in $\Delta D_{\rm B}$ appear large when compared with the value of $\Delta D_{\rm B}$ itself. It should be noted that the detections are above 3σ and the enhanced errors are mostly due to taking the logarithm of a ratio, see equation (1), where an error of 1 per cent in the continuum detection can translate to more than a 30 per cent error in $\Delta D_{\rm B}$ (depending upon how small the difference is between the intrinsic and observed spectra).

A comparison of the $\Delta D_{\rm B}$ values determined in this work versus previous values published in the literature is shown in Fig. 8, as a consistency check. The majority of the measurements are clustered at values <0.4 mag, with literature values showing a slightly larger spread in $\Delta D_{\rm B}$ than our sample. The main source of deviation between this work and the literature can be attributed to the $T_{\rm eff}$ and $\log(g)$ parameters used for each star; as these differ so will the intrinsic spectra from which $\Delta D_{\rm B}$ is measured. The figure shows this clearly with a number of objects having deviant $\Delta D_{\rm B}$ and stellar parameters, where the largest variations in $\Delta D_{\rm B}$ are indeed the stars with the largest changes in $T_{\rm eff}$ and $\log(g)$, compared to the literature values. However, there is one star whose deviation in $\Delta D_{\rm B}$ cannot be explained by the changes in $T_{\rm eff}$ and $\log(g)$ alone. Instead, the deviations may also be compounded by genuine variability of the star and/or accretion rate. Such variability can be seen within the literature, and in single stars themselves (Pogodin et al. 2012; Mendigutía et al. 2013). Additionally, intrinsic features in the spectra can contribute to differences too; the approach in this paper uses monochromatic points from spectra, whereas the majority of comparison stars primarily use broad-band photometry. Overall, the majority of sources are in common, within the errors, and most discrepancies can be explained by the adoption of stellar parameters.

5 ACCRETION RATES

Accretion rates are an important parameter of PMS stars. They provide an insight into how the stars are evolving, along with the impact this will have on disc–star interactions, and may even have repercussions on planet formation.

5.1 Magnetospheric modelling

In this work, the measured $\Delta D_{\rm B}$ is used to calculate $\dot{M}_{\rm acc}$ using accretion shock modelling within the context of MA. This theory is adopted in order to test its applicability to a wide sample of HAeBes. The main assumption here is that the excess flux visible over the Balmer jump region is produced by shocked emission from an infalling accretion column. A detailed description of the magnetospherically driven accretion column and shock modelling is given by Calvet & Gullbring (1998, hereafter CG98), while a description of its application to HAeBe stars is given in Muzerolle et al. (2004) and Mendigutía et al. (2011b). Here we summarize the key points of those papers and detail how they work in regard to this sample.

First, the magnetic field lines of the star interact with the disc and truncate it at the truncation radius, R_i. It is generally accepted that the truncation radius is close to, or inside, the corotation radius, $R_{\rm cor}$ (Koenigl 1991; Shu et al. 1994; CG98). For this work, R_i is chosen to be 2.5 $R_\star$, as this has been shown to be an appropriate value which is often less than $R_{\rm cor}$ (Muzerolle et al. 2004; Mendigutía et al. 2011b). $R_{\rm cor}$ can be smaller than the adopted 2.5 $R_\star$, as is the case for fast rotators, but this will not affect the derived accretion rate significantly, i.e. for a very small truncation radius of $R_i = 1.5\ {\rm R}_\odot$, the resulting accretion rate would be less than a factor of 2 different from one where $R_i = 2.5\ {\rm R}_\odot$.

At the truncation radius material is funnelled by the field lines and falls at speeds close to free-fall towards the stellar surface, where it shocks the photosphere upon impact. The velocity of the infalling material, v_s, is given as

$$v_s = \left(\frac{2{\rm G}M_\star}{R_\star}\right)^{1/2}\left(1-\frac{R_\star}{R_i}\right)^{1/2}. \quad (9)$$

The velocity can be related to the accretion rate via the density. This is because $\dot{M}_{\rm acc}$ is flowing at the same rate as the velocity through an accretion column, which also covers a given area of the star. Therefore, the density can be expressed as

$$\rho = \frac{\dot{M}_{\rm acc}}{A v_s}, \quad (10)$$

where A is the area of the star covered by the accretion column, defined as $A = f4\pi R_\star^2$, and f is a filling factor such that $f = 0.1$ would be 10 per cent surface coverage. The filling factor is required as we consider the accretion to be funnelled though a column, rather than being evenly distributed over the entire stellar surface. Putting this in terms of energy, the total inward flux of energy of the accretion column is

$$\mathbf{F} = (1/2)\rho v_s^3. \quad (11)$$

This amount of energy is carried into the column and must be re-emitted back out of the star (see CG98 for details on this energy balance). This means the total luminosity from the accretion column, as given in CG98, can be written as

$$L_{\rm col} = (\mathbf{F} + F_*)A = \zeta\left(\frac{G\dot{M}_{\rm acc}M_\star}{R_\star}\right) + F_\star A = \zeta L_{\rm acc} + F_\star A, \quad (12)$$

Table 3. Table of accretion rates. Column 1 gives the target name. Columns 2–4 give the measured Balmer excess, filling factor, and derived accretion rate. $\Delta D_{\rm B}$ errors are rounded to the closest 0.01 and include all systematic errors too. Column 5 details by which method the values were obtained. Column 6 gives the accretion luminosity. Finally, column 7 notes which stars can have their excess modelled successfully by MA.

Name	$\Delta D_{\rm B}$ (mag)	f (per cent)	$\log(\dot{M}_{\rm acc})$ ($M_\odot$ yr^{-1})	Method(s) used	$\log(L_{\rm acc})$ ($L_\odot$)	Achievable by MA
UX Ori	≤ 0.04	≤ 0.7	≤ -7.26	Methods 1 and 2	≤ 0.13	y
PDS 174	≤ 0.02	≤ 2.8	≤ -6.76	Method 2	≤ 0.92	y
V1012 Ori	$0.19^{+0.05}_{-0.05}$	$4.4^{+1.0}_{-0.9}$	$-7.20^{+0.21}_{-0.28}$	Methods 1 and 2	$0.35^{+0.26}_{-0.32}$	y
HD 34282	$0.06^{+0.05}_{-0.05}$	$1.7^{+0.9}_{-0.8}$	$-7.69^{+0.28}_{-0.59}$	Method 1	$-0.06^{+0.32}_{-0.61}$	y
HD 287823	$0.15^{+0.05}_{-0.05}$	$3.0^{+0.7}_{-0.7}$	$-7.13^{+0.18}_{-0.23}$	Methods 1 and 2	$0.37^{+0.20}_{-0.24}$	y
HD 287841	≤ 0.05	≤ 0.8	≤ -7.82	Methods 1 and 2	≤ -0.32	y
HD 290409	≤ 0.07	≤ 2.1	≤ -7.31	Methods 1 and 2	≤ 0.25	y
HD 35929	$0.10^{+0.05}_{-0.05}$	$1.0^{+0.4}_{-0.3}$	$-6.37^{+0.18}_{-0.26}$	Methods 1 and 2	$0.87^{+0.20}_{-0.28}$	y
HD 290500	$0.21^{+0.05}_{-0.05}$	$6.1^{+1.7}_{-1.5}$	$-6.11^{+0.17}_{-0.17}$	Methods 1 and 2	$1.29^{+0.35}_{-0.21}$	y
HD 244314	$0.12^{+0.05}_{-0.05}$	$2.4^{+0.7}_{-0.7}$	$-7.12^{+0.20}_{-0.25}$	Methods 1 and 2	$0.35^{+0.21}_{-0.26}$	y
HK Ori	$0.66^{+0.05}_{-0.05}$	$27.7^{+6.0}_{-3.8}$	$-6.17^{+0.17}_{-0.16}$	Methods 1 and 2	$1.33^{+0.19}_{-0.18}$	y
HD 244604	$0.05^{+0.05}_{-0.05}$	$1.1^{+0.7}_{-0.1}$	$-7.22^{+0.26}_{-0.32}$	Method 1	$0.22^{+0.28}_{-0.34}$	y
UY Ori	≤ 0.02	≤ 0.6	≤ -7.92	Methods 1 and 2	≤ -0.35	y
HD 245185	≤ 0.07	≤ 2.3	≤ -7.29	Methods 1 and 2	≤ 0.29	y
T Ori	≤ 0.05	≤ 1.0	≤ -6.54	Methods 1 and 2	≤ 0.79	y
V380 Ori	$0.87^{+0.05}_{-0.05}$	$80.3^{+19.7}_{-21.9}$	$-5.34^{+0.10}_{-0.15}$	Methods 1 and 2	$2.12^{+0.31}_{-0.16}$	y
HD 37258	$0.14^{+0.05}_{-0.05}$	$4.5^{+1.5}_{-1.3}$	$-6.98^{+0.14}_{-0.17}$	Methods 1 and 2	$0.58^{+0.15}_{-0.18}$	y
HD 290770	$0.15^{+0.05}_{-0.05}$	$6.2^{+1.6}_{-1.5}$	$-6.74^{+0.12}_{-0.14}$	Methods 1 and 2	$0.82^{+0.16}_{-0.17}$	y
BF Ori	$0.15^{+0.05}_{-0.05}$	$3.6^{+0.9}_{-0.9}$	$-6.65^{+0.17}_{-0.25}$	Method 2	$0.77^{+0.19}_{-0.27}$	y
HD 37357	$0.30^{+0.05}_{-0.05}$	$10.1^{+1.7}_{-1.5}$	$-6.42^{+0.09}_{-0.06}$	Methods 1 and 2	$1.08^{+0.09}_{-0.06}$	y
HD 290764	$0.21^{+0.05}_{-0.05}$	$3.5^{+0.8}_{-0.7}$	$-6.56^{+0.17}_{-0.22}$	Methods 1 and 2	$0.80^{+0.21}_{-0.24}$	y
HD 37411	$0.15^{+0.05}_{-0.05}$	$4.9^{+1.3}_{-1.2}$	$-7.13^{+0.24}_{-0.34}$	Methods 1 and 2	$0.47^{+0.29}_{-0.38}$	y
V599 Ori	≤ 0.01	≤ 0.1	≤ -7.67	Method 2	≤ -0.33	y
V350 Ori	$0.15^{+0.05}_{-0.05}$	$3.7^{+1.0}_{-0.9}$	$-6.95^{+0.18}_{-0.23}$	Methods 1 and 2	$0.55^{+0.19}_{-0.24}$	y
HD 250550	$0.30^{+0.05}_{-0.05}$	$17.1^{+4.3}_{-3.1}$	$-5.63^{+0.14}_{-0.11}$	Methods 1 and 2	$1.82^{+0.32}_{-0.17}$	y
V791 Mon	$0.19^{+0.05}_{-0.05}$	$27.5^{+10.2}_{-8.0}$	$-6.16^{+0.28}_{-0.35}$	Methods 1 and 2	$1.55^{+0.32}_{-0.39}$	y
PDS 124	$0.11^{+0.05}_{-0.05}$	$4.1^{+1.3}_{-1.2}$	$-7.11^{+0.13}_{-0.19}$	Method 2	$0.50^{+0.14}_{-0.20}$	y
LkHa 339	$0.13^{+0.05}_{-0.05}$	$5.3^{+1.5}_{-2.1}$	$-6.81^{+0.12}_{-0.22}$	Method 2	$0.75^{+0.13}_{-0.22}$	y
VY Mon	$0.23^{+0.14}_{-0.14}$	$17.5^{+22.7}_{-13.0}$	$-5.50^{+0.42}_{-0.64}$	Methods 1 and 2	$1.96^{+0.60}_{-0.66}$	y
R Mon	$0.86^{+0.05}_{-0.05}$	–	–	Methods 1 and 2	–	n
V590 Mon	–	–	–	–	–	–
PDS 24	≤ 0.05	≤ 1.9	≤ -7.25	Method 2	≤ 0.31	y
PDS 130	$0.16^{+0.05}_{-0.05}$	$6.6^{+1.6}_{-1.5}$	$-6.23^{+0.12}_{-0.13}$	Methods 1 and 2	$1.22^{+0.17}_{-0.15}$	y
PDS 229N	$0.09^{+0.05}_{-0.05}$	$6.4^{+2.4}_{-3.6}$	$-6.67^{+0.14}_{-0.36}$	Method 2	$0.96^{+0.14}_{-0.36}$	y
GU CMa	$0.14^{+0.05}_{-0.05}$	$60.3^{+33.4}_{-18.5}$	$-5.00^{+0.23}_{-0.13}$	Methods 1 and 2	$2.72^{+0.41}_{-0.36}$	y
HT CMa	$0.11^{+0.05}_{-0.05}$	$4.3^{+1.5}_{-1.4}$	$-6.61^{+0.16}_{-0.19}$	Methods 1 and 2	$0.89^{+0.20}_{-0.19}$	y
Z CMa	$1.08^{+0.05}_{-0.05}$	$48.0^{+17.0}_{-9.4}$	$-3.01^{+0.20}_{-0.19}$	Methods 1 and 2	$4.05^{+0.22}_{-0.22}$	y
HU CMa	$0.14^{+0.05}_{-0.05}$	$12.2^{+3.4}_{-4.9}$	$-6.35^{+0.11}_{-0.22}$	Methods 1 and 2	$1.27^{+0.11}_{-0.22}$	y
HD 53367	$0.10^{+0.05}_{-0.05}$	–	–	Methods 1 and 2	–	n
PDS 241	$0.05^{+0.05}_{-0.05}$	$21.6^{+20.3}_{-1.3}$	$-5.56^{+0.29}_{-0.06}$	Methods 1 and 2	$2.25^{+0.37}_{-0.23}$	y
NX Pup	$0.08^{+0.05}_{-0.05}$	$0.9^{+0.4}_{-0.3}$	$-6.96^{+0.21}_{-0.33}$	Method 2	$0.34^{+0.23}_{-0.34}$	y
PDS 27	$0.17^{+0.13}_{-0.16}$	$40.0^{+55.0}_{-39.0}$	$-3.96^{+0.76}_{-1.32}$	Methods 1 and 2	$3.49^{+0.78}_{-0.82}$	y
PDS 133	$1.26^{+0.05}_{-0.05}$	–	–	Methods 1 and 2	–	n
HD 59319	$0.05^{+0.05}_{-0.05}$	$3.4^{+2.3}_{-0.4}$	$-5.76^{+0.22}_{-0.11}$	Methods 1 and 2	$1.65^{+0.26}_{-0.15}$	y
PDS 134	≤ 0.03	≤ 3.0	≤ -5.60	Method 2	≤ 1.82	y
HD 68695	$0.05^{+0.05}_{-0.05}$	$1.3^{+0.8}_{-0.1}$	$-7.78^{+0.30}_{-0.38}$	Method 2	$-0.17^{+0.34}_{-0.41}$	y
HD 72106	$0.31^{+0.05}_{-0.05}$	$7.7^{+1.4}_{-1.3}$	$-6.21^{+0.15}_{-0.18}$	Methods 1 and 2	$1.20^{+0.18}_{-0.20}$	y
TYC 8581-2002-1	$0.15^{+0.05}_{-0.05}$	$4.6^{+1.2}_{-1.0}$	$-6.58^{+0.10}_{-0.13}$	Methods 1 and 2	$0.88^{+0.11}_{-0.13}$	y

Table 3 – *continued.*

Name	$\Delta D_{\rm B}$ (mag)	f (per cent)	$\log(\dot{M}_{\rm acc})$ ($M_\odot$ yr^{-1})	Method(s) used	$\log(L_{\rm acc})$ ($L_\odot$)	Achievable by MA
PDS 33	≤ 0.04	≤ 1.2	≤ -7.84	Methods 1 and 2	$\leq$ -0.21	y
HD 76534	≤ 0.01	≤ 1.7	≤ -6.95	Methods 1 and 2	≤ 0.77	y
PDS 281	–	–	–	–	–	–
PDS 286	$0.07^{+0.05}_{-0.05}$	$64.6^{+35.4}_{-39.6}$	$-5.41^{+0.20}_{-0.69}$	Methods 1 and 2	$2.55^{+0.62}_{-0.71}$	y
PDS 297	≤ 0.01	≤ 0.4	≤ -7.60	Method 2	≤ -0.12	y
HD 85567	$0.55^{+0.05}_{-0.05}$	–	–	Methods 1 and 2	–	n
HD 87403	$0.05^{+0.05}_{-0.05}$	$1.5^{+0.9}_{-0.2}$	$-5.82^{+0.20}_{-0.07}$	Method 2	$1.48^{+0.21}_{-0.09}$	y
PDS 37	$0.16^{+0.22}_{-0.15}$	$40.0^{+54.0}_{-39.0}$	$-3.56^{+0.60}_{-1.62}$	Method 1	$3.85^{+0.65}_{-1.62}$	y
HD 305298	$0.06^{+0.05}_{-0.05}$	–	–	Method 2	–	n
HD 94509	–	–	–	–	–	–
HD 95881	≤ 0.05	≤ 1.5	≤ -5.65	Methods 1 and 2	≤ 1.63	y
HD 96042	$0.12^{+0.05}_{-0.05}$	$94.4^{+5.6}_{-38.5}$	$-4.57^{+0.03}_{-0.28}$	Methods 1 and 2	$3.18^{+0.32}_{-0.30}$	y
HD 97048	≤ 0.01	≤ 0.4	≤ -8.16	Method 2	≤ -0.55	y
HD 98922	≤ 0.01	≤ 0.4	≤ -6.97	Method 2	≤ 0.41	y
HD 100453	≤ 0.01	≤ 0.1	≤ -8.31	Methods 1 and 2	≤ -0.92	y
HD 100546	$0.18^{+0.05}_{-0.05}$	$6.1^{+1.6}_{-1.5}$	$-7.04^{+0.13}_{-0.15}$	Methods 1 and 2	$0.56^{+0.14}_{-0.15}$	y
HD 101412	≤ 0.04	≤ 1.2	≤ -7.61	Methods 1 and 2	≤ -0.04	y
PDS 344	≤ 0.03	≤ 3.5	≤ -7.02	Methods 1 and 2	≤ 0.68	y
HD 104237	$0.17^{+0.05}_{-0.05}$	$2.8^{+0.7}_{-0.6}$	$-6.68^{+0.15}_{-0.20}$	Methods 1 and 2	$0.70^{+0.18}_{-0.22}$	y
V1028 Cen	$0.10^{+0.05}_{-0.05}$	$10.6^{+3.7}_{-3.3}$	$-5.76^{+0.16}_{-0.22}$	Method 1	$1.76^{+0.26}_{-0.24}$	y
PDS 361S	$0.12^{+0.05}_{-0.05}$	$26.2^{+9.9}_{-7.7}$	$-5.26^{+0.17}_{-0.20}$	Methods 1 and 2	$2.35^{+0.27}_{-0.23}$	y
HD 114981	≤ 0.06	≤ 8.1	≤ -5.48	Methods 1 and 2	≤ 2.03	y
PDS 364	$0.28^{+0.05}_{-0.05}$	$26.8^{+8.4}_{-6.4}$	$-6.05^{+0.13}_{-0.12}$	Methods 1 and 2	$1.58^{+0.13}_{-0.12}$	y
PDS 69	$0.31^{+0.05}_{-0.05}$	$62.8^{+29.8}_{-20.8}$	$-5.32^{+0.21}_{-0.21}$	Methods 1 and 2	$2.28^{+0.30}_{-0.27}$	y
DG Cir	$0.79^{+0.05}_{-0.05}$	–	–	Methods 1 and 2	–	n
HD 132947	$0.06^{+0.05}_{-0.05}$	$2.1^{+1.0}_{-1.0}$	$-6.71^{+0.17}_{-0.42}$	Methods 1 and 2	$0.73^{+0.18}_{-0.42}$	y
HD 135344B	$0.07^{+0.05}_{-0.05}$	$0.7^{+0.3}_{-0.3}$	$-7.37^{+0.24}_{-0.41}$	Methods 1 and 2	$-0.04^{+0.26}_{-0.42}$	y
HD 139614	$0.09^{+0.05}_{-0.05}$	$1.5^{+0.6}_{-0.5}$	$-7.63^{+0.20}_{-0.30}$	Method 1	$-0.10^{+0.21}_{-0.31}$	y
PDS 144S	≤ 0.01	≤ 0.1	≤ -8.35	Method 1	≤ -0.90	y
HD 141569	$0.05^{+0.05}_{-0.05}$	$1.5^{+0.9}_{-0.1}$	$-7.65^{+0.33}_{-0.47}$	Method 1	$-0.05^{+0.37}_{-0.50}$	y
HD 141926	$0.20^{+0.05}_{-0.05}$	–	–	Methods 1 and 2	–	n
HD 142666	≤ 0.01	≤ 0.1	≤ -8.38	Methods 1 and 2	≤ -0.93	y
HD 142527	$0.06^{+0.05}_{-0.05}$	$0.6^{+0.3}_{-0.3}$	$-7.45^{+0.19}_{-0.48}$	Method 1	$-0.09^{+0.19}_{-0.48}$	y
HD 144432	$0.07^{+0.05}_{-0.05}$	$1.0^{+0.5}_{-0.4}$	$-7.38^{+0.22}_{-0.40}$	Methods 1 and 2	$0.02^{+0.24}_{-0.41}$	y
HD 144668	$0.20^{+0.05}_{-0.05}$	$3.9^{+0.9}_{-0.8}$	$-6.25^{+0.16}_{-0.19}$	Methods 1 and 2	$1.10^{+0.19}_{-0.22}$	y
HD 145718	≤ 0.01	≤ 0.2	≤ -8.51	Method 1	≤ -1.01	y
PDS 415N	≤ 0.04	≤ 0.5	≤ -8.45	Methods 1 and 2	≤ -0.91	y
HD 150193	$0.07^{+0.05}_{-0.05}$	$1.6^{+0.8}_{-0.7}$	$-7.45^{+0.25}_{-0.43}$	Method 2	$0.10^{+0.26}_{-0.44}$	y
AK Sco	≤ 0.04	≤ 0.4	≤ -7.90	Method 1	≤ -0.52	y
PDS 431	$0.11^{+0.05}_{-0.05}$	$4.3^{+1.5}_{-1.4}$	$-6.06^{+0.16}_{-0.22}$	Methods 1 and 2	$1.34^{+0.21}_{-0.24}$	y
KK Oph	≤ 0.05	≤ 1.0	≤ -7.84	Method 2	≤ -0.29	y
HD 163296	$0.07^{+0.05}_{-0.05}$	$1.8^{+0.8}_{-0.8}$	$-7.49^{+0.14}_{-0.30}$	Method 2	$0.08^{+0.14}_{-0.30}$	y
MWC 297	$0.11^{+0.08}_{-0.08}$	$56.3^{+43.7}_{-26.5}$	$-5.16^{+0.25}_{-0.43}$	Methods 1 and 2	$2.62^{+0.40}_{-0.48}$	y

where $F_\star$ is the intrinsic flux of the stellar photosphere, $L_{\rm acc}$ is the accretion luminosity, and $\zeta = 1 - (R_\star/R_i)$. The accretion luminosity is defined as $L_{\rm acc} = G\dot{M}_{\rm acc}M_\star/R_\star$.

As shown in Mendigutía et al. (2011b), the column luminosity is $L_{\rm col} = F_{\rm col}A$, where $F_{\rm col}$ is the flux produced by the accretion column. This total amount of flux can be expressed as a blackbody function, where $F_{\rm col} = \sigma T_{\rm col}^4$. Similarly, the same can be done for the photosphere, $F_* = \sigma T_*^4$. This results in $\sigma T_{\rm col}^4 = \mathbf{F} + \sigma T_\star^4$.

At this point, the unknowns are f, $\mathbf{F}$, $T_{\rm col}$, and $\dot{M}_{\rm acc}$. $T_{\rm col}$ has just been shown to be governed by the amount of energy flowing on to the photosphere, $\mathbf{F}$, and by the temperature of the photosphere itself, $T_\star$. For each star, $T_{\rm col}$ is determined using the temperatures

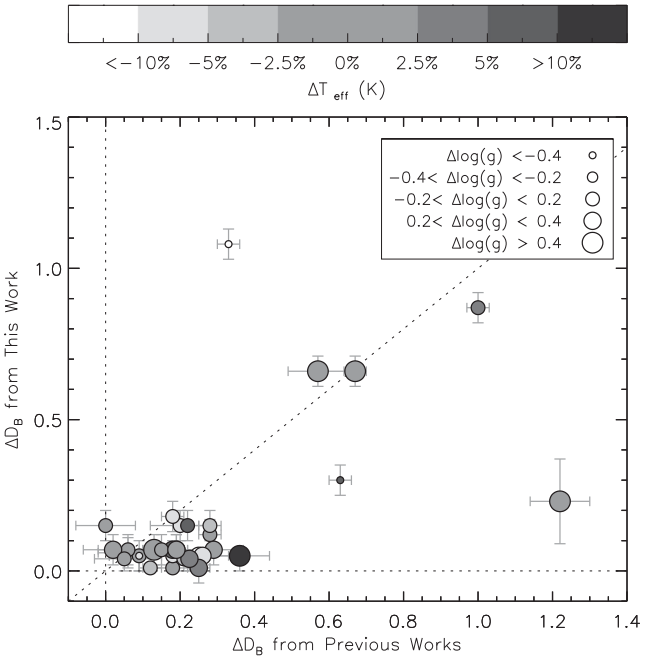

Figure 8. A comparison is drawn here between the final $\Delta D_{\rm B}$ measured in this work versus the $\Delta D_{\rm B}$ measured by other authors in the literature (Donehew & Brittain 2011; Mendigutía et al. 2011b; Pogodin et al. 2012). The difference in temperature between the two sources is calculated as a percentage of the total stellar temperature (cooler temperatures than the literature are white, while hotter ones are black). The size of each symbol reflects the difference in log(g) measured. Overall, the largest deviations in $\Delta D_{\rm B}$ are for the objects with the greatest differences in stellar parameters.

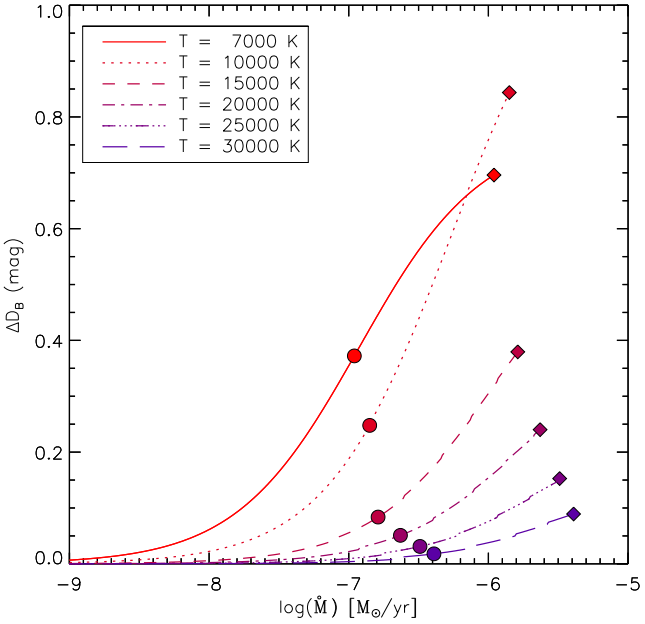

Figure 9. The relationship between $\Delta D_{\rm B}$ and $\dot{M}_{\rm acc}$ is shown here, for a series of stars with different temperatures (labelled in the legend). The stellar parameters used for each case are the ones typical for a ZAMS star of the temperature in question. It is apparent that the same $\Delta D_{\rm B}$ value would result in a higher accretion rate in hotter stars. The filled circles display the point at which $f = 0.1$, where the accretion column covers 10 per cent of the surface. Similarly, the filled diamonds are where $f = 1.0$ (full coverage). In all cases, $\mathbf{F} = 10^{12}$ erg cm^{-2} Å^{-1}.

we derived, and by fixing $\mathbf{F} = 10^{12}$ erg cm^{-2} Å^{-1}, as this has been shown to provide appropriate filling factors of $\leq$0.15 in the majority of cases in HAeBes studied so far (Muzerolle et al. 2004; Mendigutía et al. 2011b). This leaves only f and $\dot{M}_{\rm acc}$ remaining. $\dot{M}_{\rm acc}$ can be determined from $\Delta D_{\rm B}$ by making use of the equations above; for which there is a unique $\Delta D_{\rm B}$ versus $\dot{M}_{\rm acc}$ combination for each star due to its stellar parameters. To obtain this curve, $\dot{M}_{\rm acc}$ values are tested between 10^{-3} and 10^{-10} M$_\odot$ yr^{-1}. With $\mathbf{F}$ fixed, and all the other stellar parameters known, the filling factor corresponding to each $\dot{M}_{\rm acc}$ value is found through the following equation [which is a rearrangement of the second and third terms in equation (12)]:

$$f = \zeta \left(\frac{G \dot{M}_{\rm acc} M_\star}{R_\star} \right) \frac{1}{4\pi R_\star^2 \mathbf{F}}. \quad (13)$$

The $T_{\rm col}$ determined previously is used to make a blackbody, which represents the accretion hotspot, and multiplying this by f gives the excess flux. The excess flux is then combined with a KC-model, determined using the relevant stellar parameters. From this, $\Delta D_{\rm B}$ can be measured. This is repeated for all $\dot{M}_{\rm acc}$ and f combinations. The result provides a unique $\Delta D_{\rm B}$ versus $\dot{M}_{\rm acc}$ curve, which the accretion rate can be read from.

Fig. 9 gives the $\Delta D_{\rm B}$ versus $\dot{M}_{\rm acc}$ curves for a series of different temperature stars (for simplicity in the figure their other parameters are taken from the ZAMS). The figure demonstrates how the same $\Delta D_{\rm B}$, measured in two different temperature stars, can refer to wildly differing accretion rates. Also, the $T = 10\,000$ K curve has the highest $\Delta D_{\rm B}$ value as the size of the Balmer jump peaks at around this temperature.

Fig. 10 demonstrates the same concept of $\Delta D_{\rm B}$ versus $\dot{M}_{\rm acc}$ changing as a function of temperature, as shown by the curves in Fig. 9. This figure also highlights how the excess flux impacts the appearance of the spectra too. There are two cases in the figure, one for a star of 10 000 K, and the other for a star of 20 000 K. It can be seen for $\dot{M}_{\rm acc} = 10^{-6.5}$ that the resulting $\Delta D_{\rm B}$ changes from 0.41 for the 10 000 K star to only 0.17 for the 20 000 K star. This is why the calculation of separate $\Delta D_{\rm B}$ versus $\dot{M}_{\rm acc}$ curves, for each star, is crucial. It also demonstrates that the SED shape is not significantly affected by the excess longwards of 4000 Å, which means that the approach of methods 1 and 2 remains valid (as does the photometry fitting). Table 3 contains the $\dot{M}_{\rm acc}$ values for each star using an individual curve for each star.

5.2 Literature comparisons

Comparisons of $\dot{M}_{\rm acc}$ derived in this work are made against previous detections in HAeBes and CTTs. In the first comparison, Fig. 11 places this sample against other stars from the literature in which $\dot{M}_{\rm acc}$ has also been determined directly using $\Delta D_{\rm B}$. For the HAes, $\sim$10 000 K and lower, the range in this work appears similar to previous works, with $\dot{M}_{\rm acc}$ spanning from anywhere between 10^{-8} and 10^{-5} M$_\odot$ yr^{-1}, with the exception of one star at $\sim 10^{-3}$ M$_\odot$ yr^{-1} (Z CMa, which is likely a very young HBe based on its mass of 11 M$_\odot$). The HBes closest to the HAes show a similar range in magnitude of 10^{-7}–10^{-4} M$_\odot$ yr^{-1}. The scatter then decreases once the temperature has increased beyond 20 000 K, where $\dot{M}_{\rm acc}$ spans 10^{-6}–10^{-4} M$_\odot$ yr^{-1}. This decrease can be partially attributed to a detection effect; as the temperature of the star increases, the observable $\Delta D_{\rm B}$ will decrease. Therefore, if the temperature of the star is very high, then low accretion rates will be undetectable via the Balmer excess method. This is supported by the $\Delta D_{\rm B}$ versus log($\dot{M}_{\rm acc}$) curves in Fig. 9. Returning to Fig. 11, comparisons are also drawn against

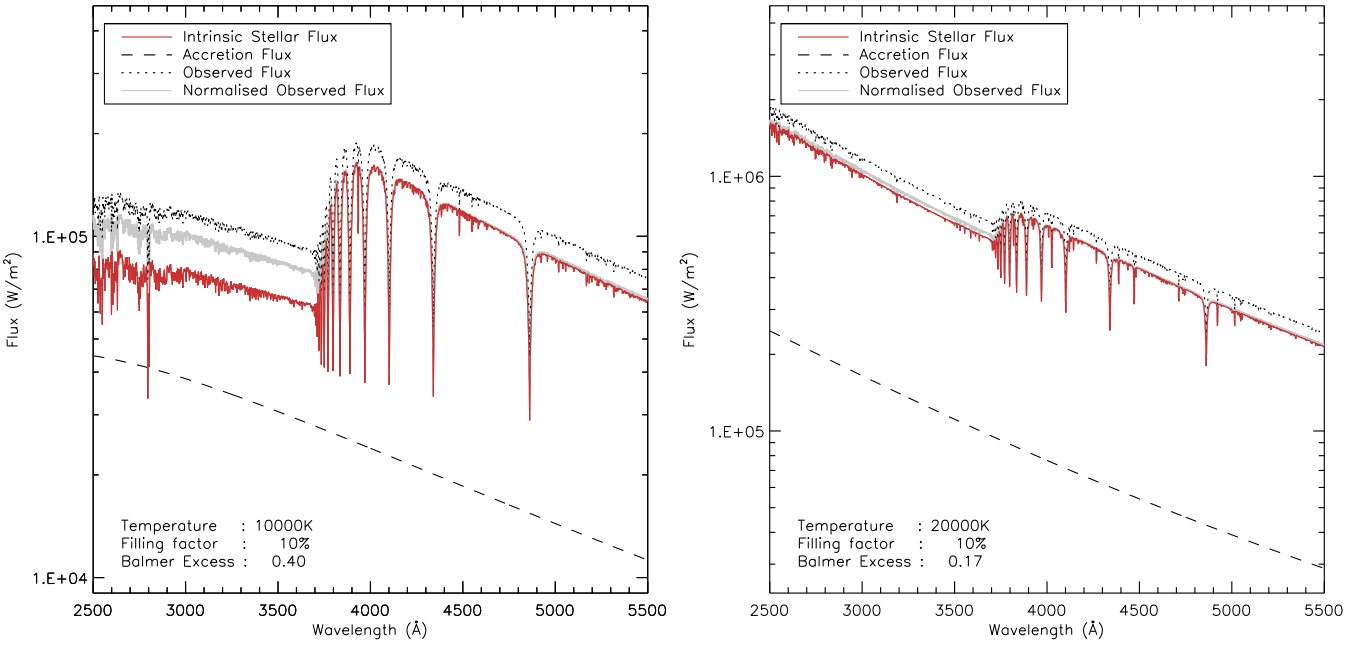

Figure 10. KC-model atmospheres (red) for a 10 000 K star, on the left, and a 20 000 K star, on the right. In both cases, $\mathbf{F} = 10^{12}$ erg cm^{-2} Å^{-1} and $\log(\dot{M}_{\rm acc}) = -6.5$. These allow the accretion flux (black dashed) to be calculated. Adding this flux to the intrinsic photosphere provides the observed spectra (black dotted). This spectrum is then normalized to 4000 Å (grey), so that its continuum matches the intrinsic between 4000 and 4600 Å, allowing $\Delta D_{\rm B}$ to be measured via the method 1 approach. The resulting $\Delta D_{\rm B}$ values are given in the plot, demonstrating how they vary depending on the temperature of the star.

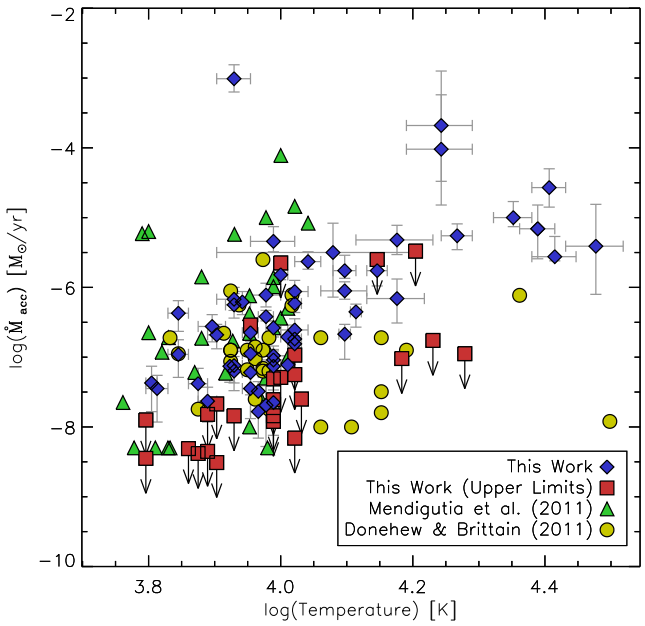

Figure 11. $\dot{M}_{\rm acc}$ versus $T_{\rm eff}$ is shown for each object, along with literature values for a comparison. In general, it can be seen that $\dot{M}_{\rm acc}$ increases with temperature, with a scatter of two to three orders of magnitude in $\dot{M}_{\rm acc}$ throughout.

previously published accretion rates. The Mendigutía et al. (2011b) sample has a slightly larger scatter showing some $\dot{M}_{\rm acc}$ detections below our findings; this can again be attributed to detection limits in this work. But it can also be seen that there are many stars in Mendigutía et al. (2011b) which have accretion rates about an order of magnitude higher than our findings. The exact reason for the discrepancies is unknown, but it is likely to be a combination of the two different types of data set, spectra and photometry, and the different methods of measurement used, i.e. the photometric method requires dereddening to be performed prior to measurement of $\Delta D_{\rm B}$. Variability may also play a role.

Comparing our results with the work of Donehew & Brittain (2011), we find a systematically higher accretion rate for objects hotter than 10 000 K, the HBes, of around one to two orders of magnitude. This can be attributed to their adoption of a single $\Delta D_{\rm B}$ versus $\dot{M}_{\rm acc}$ relationship for all of their objects. However in this work, the relationship between the two has been calculated on an individual basis for each star, based on its stellar parameters (see Fig. 9). Therefore, they are not directly comparable.

A comparison is made of $\dot{M}_{\rm acc}$ versus $M_\star$ in Fig. 12, which includes literature values too. More specifically, this comparison looks at how the results of this sample compare to the HAeBes from Mendigutía et al. (2011b), along with a look at lower luminosity CTTs from Natta et al. (2006). A trend is seen of increasing accretion rate with increasing stellar mass; the fit shown in the figure gives $\dot{M}_{\rm acc} \propto M_\star^{2.47\pm0.07}$. The position of the HAeBes obtained in this work shows agreement with the values obtained from Mendigutía et al. (2011b). However, it can be seen at around the HAe mass range, of ∼1–2.5 M⊙, that there is a dip in the trend. Whether this is due to the physical mass of the stars or is an observational effect from different sample is unclear. This dip will be discussed further in Section 6.4 in regard to the HAeBes of this sample. An investigation into the meaning of this dip, and how the relationships behave in CTTs and HAeBes, is presented in a dedicated paper by this group (Mendigutía et al. 2015). Overall, the figure shows a trend that covers a large mass range spanning low-mass CTTs to high-mass HBes, with only some slight deviation in the HAe mass range.

Fig. 13 instead shows a relationship of the luminosities instead of the mass, specifically of how $L_{\rm acc}$ changes as a function of $L_\star$. Again, comparisons are made against HAeBes and CTTs from the

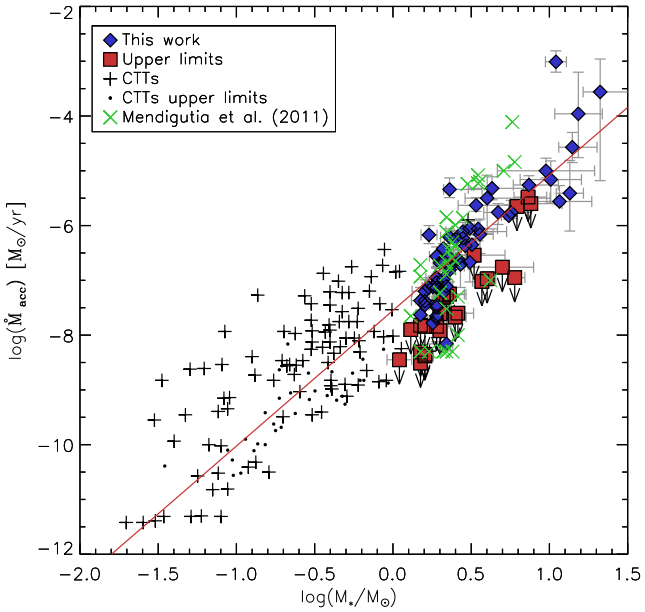

Figure 12. $\dot{M}_{\rm acc}$ versus $M_\star$ is shown for each star, where possible, along with additional HAeBe sources from Mendigutía et al. (2011b) and CTTs from Natta, Testi & Randich (2006). A red solid line fitted to all of the points, excluding upper limits, is shown of $\dot{M}_{\rm acc} \propto M_\star^{2.47\pm0.07}$.

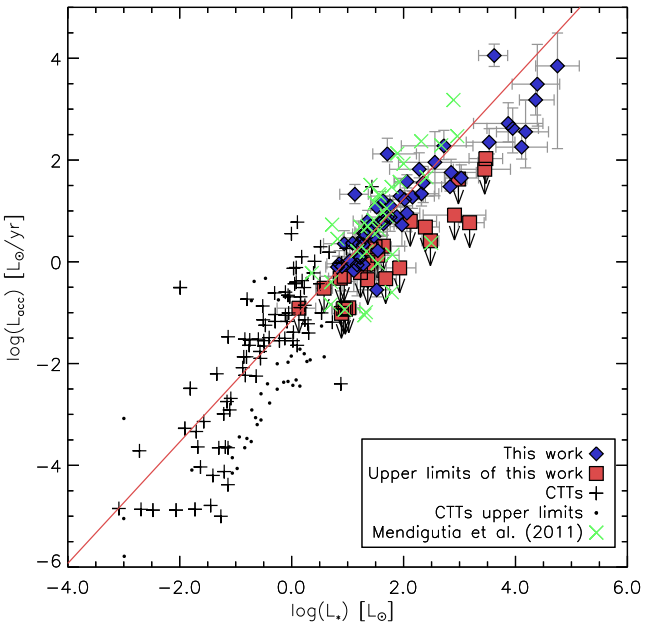

Figure 13. $L_{\rm acc}$ versus $L_\star$ is shown for each star in this work, along with additional HAeBe sources from Mendigutía et al. (2011b) and CTTs from Natta et al. (2006). A best fit is obtained of $L_{\rm acc} \propto L_\star^{1.19\pm0.03}$, which is plotted as a solid red line and excludes the upper limits.

literature. A positive correlation between the two is also seen here of $L_{\rm acc} \propto L_\star^{1.19\pm0.03}$. This trend in the data shows a scatter of around 2 dex in $L_{\rm acc}$ throughout the luminosity range covered; this scatter is comparable to the scatter in $\dot{M}_{\rm acc}$ shown in Fig. 11.

In total, accretion rates, and therefore accretion luminosities, have been calculated for 81 stars in the sample. Their values are seen to agree with previous literature estimates of accretion in HAeBes. The accretion rates obtained are observed to increase with both temperature and luminosity; this trend is seen in the literature for CTTs and HAeBes alike.

6 DISCUSSION

6.1 Overall results

$\Delta D_{\rm B}$ is clearly detected in 62 of the stars, while a further 26 stars have upper limits placed on them. The remaining three stars are measured as having a negative or zero $\Delta D_{\rm B}$. The possible reasons for this for each star are now discussed: V590 Mon is observed to have $\Delta D_{\rm B} = 0$ within the errors, which is acceptable as it may not be accreting; PDS 281 has been listed previously as a possible evolved star (Vieira et al. 2003), as such the parameters derived in this work may be incorrect based on our assumptions, and if it is evolved it is unlikely to be accreting; HD 94509 has very narrow and deep absorption lines in its spectrum which suggest it is a supergiant star with a low log(g), as supported by past observations (Stephenson & Sanduleak 1971), while such low values are not covered by our adopted model atmospheres. Further investigation into the accretion properties of these three stars through emission lines will be presented in a future paper by the authors, though their questionable nature as PMS objects should be noted.

There are seven objects for which the measured $\Delta D_{\rm B}$ value cannot be reproduced though MA shock modelling, using the method we adopt. This is because the appropriate $\Delta D_{\rm B}$ versus $\dot{M}_{\rm acc}$ curve calculated for each of the stars, based on its stellar parameters, cannot reach the observed $\Delta D_{\rm B}$ before a 100 per cent filling factor is achieved (see Fig. 9 for the points at which a 100 per cent filling factor is seen for different temperatures). Within this subset, three stars have a very large $\Delta D_{\rm B}$ of >0.85 (PDS 133, R Mon, and DG Cir), three have temperatures exceeding 20 000 K (HD 141926, HD 53367, and HD 305298), while the final star lies in between these two scenarios having a strong $\Delta D_{\rm B}$ value and is mid-B spectral type (HD 85567). These stars are all HBes.

Additionally, there are 12 stars whose measured $\Delta D_{\rm B}$ are modelled by filling factors of greater than 25 per cent of the stellar surface. This is allowed, but it is an unusual occurrence under MA (Valenti, Basri & Johns 1993; Long et al. 2011). A filling factor greater than 1 is an unphysical value, as it implies that the accretion column covers more than the total surface area of the star. This suggests that the MA scenario adopted here needs to be revised, or discarded, for the stars with unphysical filling factors. Caution should be exercised when considering the $\dot{M}_{\rm acc}$ values of stars with high filling factors. This amounts to 9 per cent of $\Delta D_{\rm B}$ detections being non-reproducible through the adopted MA shock modelling, with a further 15 per cent having unusually high filling factors. All of this gives a possible indication that MA may not be applicable in all HAeBes, particularly for stars with a large $\Delta D_{\rm B}$, or which have high temperatures, i.e. the HBes. The remaining 76 per cent can be fitted successfully within the context of MA.

6.2 HR-diagram

Using the spectra, log(g) could be determined for the majority of the sample in addition to $T_{\rm eff}$; for these stars, their stellar parameters were determined using PMS tracks. Their placement on these tracks confirms the young nature of these stars and is shown in Fig. 14, in the left-hand panel, while the right-hand panel shows the corresponding Hertzsprung-Russel-diagram. The stars which required revised distances to be calculated for them (see Section 3.3) are not included in Fig. 14 as their placement is artificial compared to the

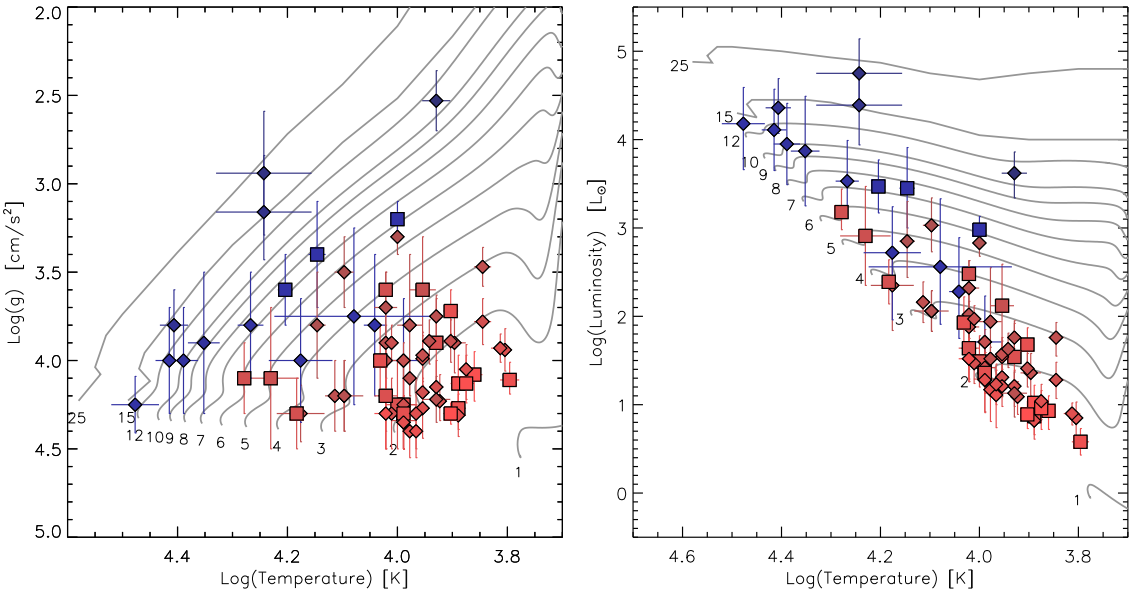

Figure 14. The left-hand panel shows all the stars for which log(g) and $T_{\rm eff}$ could be determined from the spectra. These are translated into an HR-diagram in the right-hand panel. In both panels, the colour of the points reflects the strength of the accretion rate determined in each star; dark-blue symbols are the strongest accretors, while light-red ones are the weakest accretors. The squares denote objects where $\dot{M}_{\rm acc}$ is an upper limit. The PMS evolutionary mass tracks of Bressan et al. (2012) and Bernasconi & Maeder (1996) are also plotted as solid grey lines, and are labelled according to mass. Stars which were moved on to the ZAMS are not included in this plot.

Table 4. Compares the number of HAeBes found in different mass bins with the theoretical IMF distribution.

Mass bin	Theoretical	This work
1–2 $M_{\odot}$	99	31[a]
2–4 $M_{\odot}$	39	36
4–8 $M_{\odot}$	15	11
8–16 $M_{\odot}$	6	11
>16 $M_{\odot}$	4	2

[a]This sample is focused on HAeBes and does not represent the 1–2 $M_{\odot}$ bin well, as HAeBes are generally more massive.

other stars. A large proportion of the sample are clustered between 2 and 3 $M_{\odot}$, which is likely caused by a combination of two effects. The first being that lower mass sources are more numerous, as described by the initial mass function, IMF (Salpeter 1955). The range of masses determined in this work agrees fairly well with a typical Salpeter IMF distribution, particularly when considering the selection criteria (the criteria skew our sample towards high-mass objects, as these are the ones of greater interest in this work). Table 4 shows the comparison of the mass distribution in this work versus the distribution given in Zinnecker & Yorke (2007) for a typical IMF function.

The second aspect, which may be contributing to the clustering, is a visibility effect due to low-mass stars being more evolved and less extinct than younger high-mass stars (as predicted by a comparison between the Kelvin–Helmholtz time-scale and the free-fall time-scale). This second point is supported by the A_V values measured in this sample where, in general, the lower mass objects tend to have lower A_V values. However, it should be noted that a high A_V does not necessarily mean that the HAeBe has a high mass, as many low-mass stars of young ages also have high extinction values (e.g. V599 Ori has $A_V = 4.65$, but only has $T_{\rm eff} = 8000$ K and $M_{\star} = 2.5$ $M_{\odot}$). Another point to note is that clustering of the stars in the figure could be attributed to the stars actually belonging to the same cluster. The main star-forming regions in which some of the HAeBes in this work appear to be associated with are the Orion-OB1, Mon-OB1, CMa-R1, and Sco-OB2 regions (de Zeeuw et al. 1999; Shevchenko et al. 1999; Dahm & Simon 2005; van Leeuwen 2007). Since the regions are located at fixed distances, clustering of luminosities will occur if the stars are of similar spectral type. It is worth noting that the number of stars in each mass bin of a cluster is governed by the initial mass of the cloud in which they form. By looking at just a few star-forming regions, we naturally get clusters of similar mass stars in each one, resulting in clustered regions in an HR-diagram. However, only a small number of distances are adopted from the literature as an input parameter in this work, and they are drawn from various catalogues and regions on the sky. The spread on the HR-diagram can simply be attributed to relatively low number statistics.

6.3 Age

Next, the ages of the stars are investigated. Generally for PMS stars, the higher the mass, the younger the object is. Fig. 15 shows age against temperature ($T_{\rm eff}$ is roughly proportional to $M_{\star}$ for MS stars and stars close to the ZAMS). The plot shows an inverse relationship between age and temperature where the increase in temperature results in younger ages. This is as expected as the hot objects, which evolve faster, will move away from the PMS stage of their lives quicker than the lower mass stars, allowing the higher mass stars only to be seen at an early age. This point is worth stressing when it comes to looking at HAeBes statistically, as the HBes will always be much younger than the majority of HAes, but they can also be much closer to the MS, as this is relative to their mass.

Fig. 16 shows how $\dot{M}_{\rm acc}$ changes with the age of a star. As the age increases, the accretion rate diminishes, much like what has been seen for the temperature. A fit to the data provides a relationship of

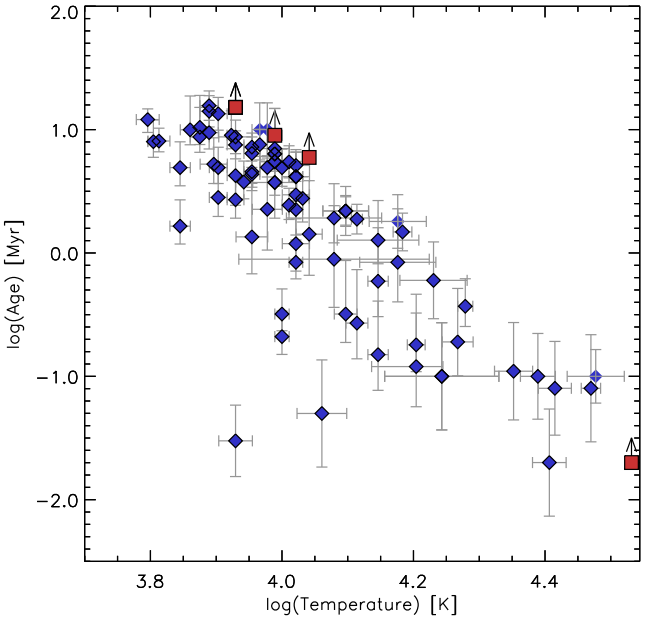

Figure 15. The PMS tracks in Fig. 14 are used to obtain an age for each star. The ages determined are plotted here against the temperature of the star. The plot shows how the older stars are always the cooler stars, i.e. the ones with a lower mass, which evolve towards the MS slower than their high-mass counter parts, as expected. However, all of the hottest objects, $T_\star > 20\,000$ K, are seen to be the youngest ones, age <0.5 Myr. Some cool and young stars are also present, which are likely to be in the early stages of their PMS evolution.

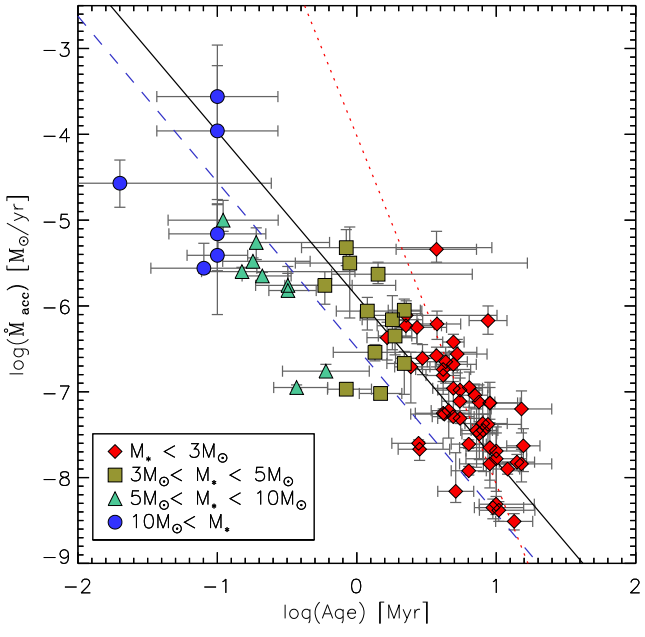

Figure 16. Plotted here are the derived accretion rates, from Table 3, against the age of the star, in a log–log plot. Various mass bins are noted by symbol and colour. Various fits are made to the different mass bins. All of the HAes are shown in red (<3 $M_\odot$), and can be fitted by a relationship of $\dot{M}_{\rm acc} \propto t^{-4.06\pm0.53}$, shown as a dotted red line; the remaining HBes (>3 $M_\odot$) are all fitted with the dashed blue line where $\dot{M}_{\rm acc} \propto t^{-1.93\pm0.24}$. Finally, a fit to all of the HAeBes is shown in black of $\dot{M}_{\rm acc} \propto t^{-1.92\pm0.09}$. Z CMa has been excluded from this fit (see the text for discussion).

$\dot{M}_{\rm acc} \propto t^{-\eta}$, where t is the age in Myrs and $\eta = 1.92 \pm 0.09$. The figure also shows the stars split into separate mass bins too. A fit to just the HBes, where $M_\star > 3$ $M_\odot$, gives $\eta = 1.93 \pm 0.24$, which is very similar to the result for all of the HAeBes, only slightly offset. However, for the HAes alone in this work, a much steeper relationship is obtained of $\eta = 4.06 \pm 0.53$. The HAeBes as a whole, and the HBe case, agree with the HAeBes investigated in the work of Mendigutía et al. (2012), where the authors obtain $\eta = 1.8$. For CTTs, a relationship has been observed where $\eta = 1.5$–2.8 (Hartmann et al. 1998). This range also encompasses the case for the HAeBes as a whole and the HBes. However, more recent studies suggest that the relationship for CTTs is actually lower than this, where $\eta = 1.2$ (Sicilia-Aguilar, Henning & Hartmann 2010; Caratti o Garatti et al. 2012), which suggests that there is a difference in the $\dot{M}_{\rm acc} \propto t^{-\eta}$ relationship between the CTTs and the HAeBes. Some caution should be noted for the ages of the HBes as their ages are less accurate than the HAes, since the HBes are younger. In particular, there are some stars which are suspected to have ages <1 Myr; the uncertainty in the ages of these stars are taken into account in the fitting.

Overall, these relationships indicate that $\dot{M}_{\rm acc}$ could be an evolutionary property of HAeBes, which decreases as the star evolves, possibly accreting all of its material or dispersing its disc with time. Modelling of disc dispersion through photoevaporation suggests that the disc lifetimes are indeed shorter for more massive stars (Gorti & Hollenbach 2009). This offers an explanation for the steep exponent observed in the HAes, in which we could be observing the transition stage of disc dispersion as they approach the MS, resulting in a decreased accretion rate. The HBes, on the other hand, are younger and may not be dispersing their disc yet, which allows them to retain a more shallow relationship between $\dot{M}_{\rm acc}$ and age.

6.4 Accretion rate versus stellar parameters

Moving on from the age, the next natural questions are: how is $\dot{M}_{\rm acc}$ related to the stellar parameters of the star; and are they influenced by it or vice versa? In Fig. 17, a comparison is made between $\dot{M}_{\rm acc}$ and $T_{\rm eff}$. The scatter in $\dot{M}_{\rm acc}$ remains constant at about two orders of magnitude throughout. There is one object, Z CMa, which can be seen as an outlier from the general scatter. This star is cool, 8500 K, very massive, $M_\star = 11$ $M_\odot$, and has a very large Balmer excess, $\Delta D_{\rm B} = 1.05$. Its placement on the HR-diagram and PMS tracks puts it at a very early stage of evolution, in which it appears to be able to accrete at large rates. This star appears to be an exception to the majority of other stars and is excluded in all fitting because of this. The overall trend is that $\dot{M}_{\rm acc}$ increases steadily with temperature; the temperature of a star is generally proportional to its mass leading to the next relationship.

Fig. 18 compares the $\log(\dot{M}_{\rm acc})$ versus $\log(M_\star)$ relationship, along with a series of fits to the data. In the figure, the stars are split into two groups, the HAes and the HBes, which comprise 60 and 40 per cent, respectively, of the total sample (the split between the two regimes is made at 3 $M_\odot$). A best fit to the HAes is made of $\dot{M}_{\rm acc} \propto M_\star^{8.59\pm1.40}$, while for the HBes a shallower relationship of $\dot{M}_{\rm acc} \propto M_\star^{2.82\pm0.41}$ is seen. An overall fit to the HAeBes is obtained of $\dot{M}_{\rm acc} \propto M_\star^{3.72\pm0.27}$, which lies between the HAe and HBe regime and favours the HBe case, which covers a greater mass distribution. When considering the HAeBes as a whole, the relationship found between $\dot{M}_{\rm acc}$ and $M_\star$ is a factor of ∼2.0 larger in exponent than in low-mass PMS stars, where $\dot{M}_{\rm acc} \propto M_\star^{2.0\pm0.2}$ (Muzerolle et al. 2005; Natta et al. 2006). The trend we observe of a steeper relationship between

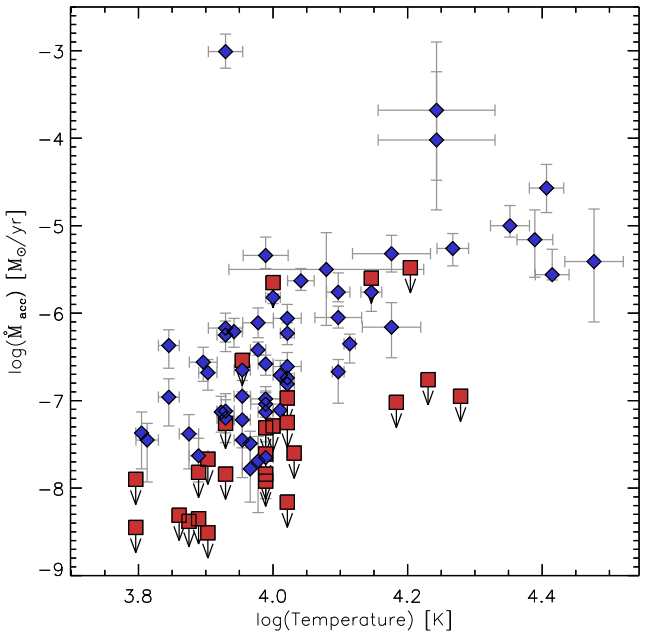

Figure 17. $\dot{M}_{\rm acc}$ is shown versus $T_{\rm eff}$ in a log–log plot here, where $\dot{M}_{\rm acc}$ appears to be increasing steadily with increasing temperature. The red squares denote upper limits. The outlier at $\log(\dot{M}_{\rm acc}) \sim -3.0$ and $\log(T_{\rm eff}) \sim 3.95$ is Z CMa.

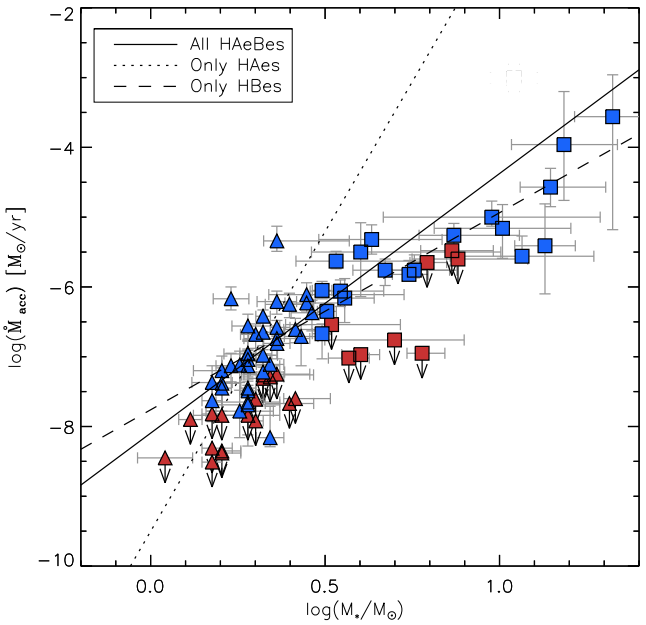

Figure 18. $\dot{M}_{\rm acc}$ versus $M_\star$ is plotted here, for all stars in which $\dot{M}_{\rm acc}$ could be determined. The stars are split into HAes (as triangles, where $M_\star < 3\,{\rm M}_\odot$) and HBes (as squares, where $M_\star > 3\,{\rm M}_\odot$). Upper limits are denoted as the points in red with downward arrows from them. Separate fits are made to the HAes, HBes, and the group as a whole, of the form $\dot{M}_{\rm acc} \propto M_\star^a$, where a is found to be 8.59 ± 1.46, 2.82 ± 0.51, and 3.72 ± 0.27, respectively. A discussion of the fits is provided in the text.

accretion rate and stellar mass, over CTTs, agrees with the findings of Mendigutía et al. (2011b), who also obtained a relationship with a much steeper exponent; they obtained $\dot{M}_{\rm acc} \propto M_\star^{4.6-5.2}$. Although the exponent for the HAeBes as a whole obtained in this work

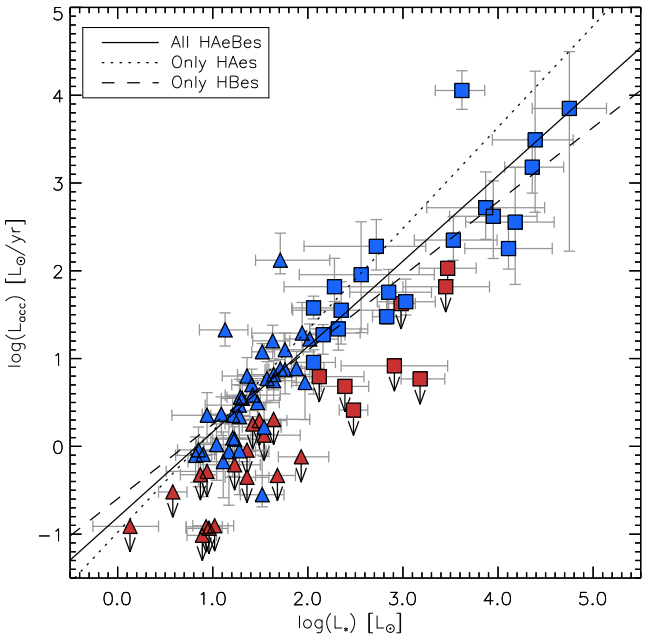

Figure 19. $L_{\rm acc}$ versus $L_\star$ is plotted here, for all stars in which $\dot{M}_{\rm acc}$ could be determined. The stars are split into HAes (as triangles, where $M_\star < 3\,{\rm M}_\odot$) and HBes (as squares, where $M_\star > 3\,{\rm M}_\odot$). Upper limits are denoted as the points in red with downward arrows from them. Separate fits are made to the HAes, HBes, and the group as a whole, of the form $L_{\rm acc} \propto L_\star^a$, where a is found to be 1.15 ± 0.20, 0.85 ± 0.12, and 0.97 ± 0.06, respectively. A discussion of the fits is provided in the text.

is slightly shallower than Mendigutía et al. (2011b), this could be attributed to our sample containing more HBes. Overall, it is apparent that HAeBes have higher accretion rates and a steeper relationship to $M_\star$ than CTTs. This could be due to HAeBes being younger stars, which are in earlier stages of accretion. The different relationships observed between HAes and HBes could be due to the HAes crossing into a transitional disc phase, in which accretion rates may be lower (see the discussion above in Section 6.3). This is also possible due to the HAes having a longer stage of evolution compared to HBes.

Alternatively, luminosities can be compared against each other instead of masses; Fig. 19 shows the luminosity plot of $\log(L_{\rm acc}/{\rm L}_\odot)$ versus $\log(L_\star/{\rm L}_\odot)$. A best fit to all the HAeBes is found of $L_{\rm acc} \propto L_\star^{0.97\pm0.06}$. This fit is in agreement with the work of Mendigutía et al. (2011b), where these authors also found a shallower relationship for HAeBes of $L_{\rm acc} \propto L_\star^{1.2}$. As in the previous comparisons presented, when looking at the masses, the HAes and HBes are divided into two groups in the figure. A best fit to the HAes is obtained of $L_{\rm acc} \propto L_\star^{1.15\pm0.20}$, which is slightly shallower than the trends seen in CTTs of $L_{\rm acc} \propto L_\star^{1.5}$ (Natta et al. 2006; Tilling et al. 2008). The HBes, on the other hand, demonstrate an even shallower relationship of $L_{\rm acc} \propto L_\star^{0.85\pm0.12}$; this is turn shifts the weighting when looking at the HAeBes as a whole. The data are suggestive of $L_{\rm acc}$ being tightly correlated with $L_\star$, but the exact relationship changes in exponent between the HAe and HBe regime.

Table 5 is provided as a condensation of the various accretion relationships extracted from the graphs. It demonstrates clearly the changes between the different mass groups when looking at accretion as either a function of mass, luminosity, or age.

Table 5. The exponents describing accretion relationships for various PMS mass groups. The relationships are of the form $A = B^C$, with C being the exponent.

Group	$\dot{M}_{\rm acc}$ versus $M_{\rm acc}$	$L_{\rm acc}$ versus $L_{\rm acc}$	$\dot{M}_{\rm acc}$ versus age
CTTs	2.00 ± 0.20	$\sim$1.50	-1.20, -1.50 to -2.80
CTTs+HAeBes	2.47 ± 0.07	1.19 ± 0.03	N/A
HAes	8.59 ± 1.46	1.15 ± 0.20	-4.06 ± 0.53
HBes	2.82 ± 0.51	0.85 ± 0.12	-1.93 ± 0.24
HAeBes	3.72 ± 0.27	0.97 ± 0.06	-1.92 ± 0.09

References for CTTs values are from: Muzerolle et al. (2005), Natta et al. (2006) for column 2 – Natta et al. (2006), Tilling et al. (2008) for column 3 – and Sicilia-Aguilar et al. (2010), Caratti o Garatti et al. (2012) for the first value in column 4, with Hartmann et al. (1998) for the second value.

7 CONCLUSIONS AND FINAL REMARKS

To conclude, we have presented the largest spectroscopic survey of HAeBes to date, obtaining the following results.

(i) Basic stellar parameters are determined for the whole sample, in a homogeneous fashion, by initially constraining $T_{\rm eff}$ and $\log(g)$ using some of the best spectra available for these stars. As such, the parameters are more consistent between objects, while only a handful of objects require specialist treatment. The findings are in agreement with previous works in the literature.

(ii) A UV excess, $\Delta D_{\rm B}$, is clearly detected in 62 stars of the sample, with upper limits allowed on a further 26 stars. $\dot{M}_{\rm acc}$ is determined for 81 of these stars through modelling within the context of MA. However, seven of the $\Delta D_{\rm B}$ detections cannot be reproduced in this context. These seven stars are all HBes, often with very large $\Delta D_{\rm B}$ values of $>$0.85 or high temperatures exceeding 20 000 K. This suggests a possible breakdown in the MA regime for HBes, particularly for early-type HBes.

(iii) A clear trend is observed of $\dot{M}_{\rm acc}$ increasing as a function of stellar mass. The relationship obtained is a power law of the form $\dot{M}_{\rm acc} \propto M_\star^{3.72\pm0.27}$. This is a steeper law than previously observed in CTTs, which is only $\dot{M}_{\rm acc} \propto M_\star^{2.0}$. We interpret this increased exponent, in the relationship between $\dot{M}_{\rm acc}$ and $M_\star$, for HAeBes as a possible combination of them being younger and therefore more active in formation than older CTTs. Deviations are seen between the HAes, where $\dot{M}_{\rm acc} \propto M_\star^{8.59\pm1.40}$, and the HBes, where $\dot{M}_{\rm acc} \propto M_\star^{2.82\pm0.0.41}$. An explanation could be that the HAes are crossing into a transitional disc phase, in which accretion rates may be lower.

(iv) There is also a trend between the accretion luminosity and the stellar luminosity, which is found to be $L_{\rm acc} \propto L_\star^{10.97\pm0.06}$ for the sample. This is lower than found in CTTs where $L_{\rm acc} \propto L_\star^{1.5}$ (Natta et al. 2006; Tilling et al. 2008). However, for a subset of the HAes, the relationship is much closer to the CTT case, where we observe $L_{\rm acc} \propto L_\star^{1.15\pm0.20}$. In contrast, a shallower relation of $L_{\rm acc} \propto L_\star^{0.85\pm0.12}$ is seen in the HBes. This demonstrates that the stellar luminosity of a star appears to be a good indicator of the accretion luminosity for a huge range of stellar luminosities, up to the HAe mass range, but there may be deviations in the HBe mass range.

(v) A trend is also seen in the HAeBes between the age of the star and $\dot{M}_{\rm acc}$, where the accretion rate decreases with increasing age, characterized by the form $\dot{M}_{\rm acc} \propto t^{-\eta}$, with $\eta = 1.92 \pm 0.09$. This implies that the accretion rate decreases as stars approach the MS. However, this result is affected by two factors. The first is that the most massive stars, with the higher accretion rates, are only observable at young ages due to their rapid evolution. Secondly, the less massive stars have a longer PMS lifetime, which could allow their accretion rate to diminish within this time. These factors could explain the change in the relationship for the HAe case where $\eta = 4.06 \pm 0.53$. Overall, this suggests that the younger objects are indeed accreting at a faster rate, and that the accretion rate diminishes more quickly for older HAeBe stars, which could be a consequence of disc dissipation.

This study has led to three main findings. First, the HAeBes display relationships in accretion which are similar but different from CTTs. $\dot{M}_{\rm acc}$ is observed to have a steeper relationship with $M_\star$ than seen in CTTs, while $L_{\rm acc}$ shows a shallower relationship with $L_\star$ than the CTT case. Secondly, there are also notable differences within the HAeBe group, when separating the HAes and HBes. Most notably, the HAes display a much steeper relationship in $\dot{M}_{\rm acc}$ when related to both age and $M_\star$. In both cases, the steepness of the relationship is approximately double that seen in HBes. However, the HAes also display an $L_{\rm acc}$ relationship to $L_\star$ which is comparable to CTTs. The third, and final, finding is that multiple early-type HBes, and stars with an observable $\Delta D_{\rm B}$ of $>$0.85, cannot be modelled successfully though MA. This suggests that there is a possible change in accretion mechanisms in these stars which requires further investigation. To further these findings, the next steps are to look at emission lines which are known tracers of accretion in CTTs and test their applicability in HAeBes. This will be presented in Paper II of the series.

ACKNOWLEDGEMENTS

The authors wish to thank the referee Benjamín Montesinos for thorough and constructive comments, which have helped improve the clarity of the manuscript. JRF gratefully acknowledges a studentship from the Science and Technology Facilities Council of the UK. JDI gratefully acknowledges funding from the European Union FP7-2011 under grant agreement no. 284405. This work has made use of NASA's Astrophysics Data System; it has also made use of the SIMBAD data base, operated at CDS, Strasbourg, France.

REFERENCES

Ababakr K. M., Fairlamb J. R., Oudmaijer R. D., van den Ancker M. E., 2015, MNRAS, in press
Alecian E. et al., 2013, MNRAS, 429, 1001
Andersen J., Lindgren H., Hazen M. L., Mayor M., 1989, A&A, 219, 142
Avedisova V., 2000, Balt. Astron., 9, 569
Baines D. et al., 2004, MNRAS, 353, 697
Baines D., Oudmaijer R. D., Porter J. M., Pozzo M., 2006, MNRAS, 367, 737
Bernasconi P. A., Maeder A., 1996, A&A, 307, 829
Bouvier J., Alencar S. H. P., Harries T. J., Johns-Krull C. M., Romanova M. M., 2007, Protostars and Planets V. Univ. Arizona Press, Tucson, p. 479

Bressan A., Marigo P., Girardi L., Salasnich B., Dal Cero C., Rubele S., Nanni A., 2012, MNRAS, 427, 127
Caffau E., Ludwig H.-G., Steffen M., Freytag B., Bonifacio P., 2011, Sol. Phys., 268, 255
Calvet N., Gullbring E., 1998, ApJ, 509, 802 (CG98)
Calvet N., Muzerolle J., Briceño C., Hernández J., Hartmann L., Saucedo J. L., Gordon K. D., 2004, ApJ, 128, 1294
Canto J., Rodriguez L. F., Calvet N., Levreault R. M., 1984, ApJ, 282, 631
Caratti o Garatti A. et al., 2012, A&A, 538, A64
Cardelli J. A., Clayton G. C., Mathis J. S., 1989, ApJ, 345, 245
Carmona A., van den Ancker M. E., Audard M., Henning T., Setiawan J., Rodmann J., 2010, A&A, 517, A67
Castelli F., Kurucz R. L., 2004, preprint (astro-ph/0405087)
Catala C. et al., 2007, A&A, 462, 293
Cauley P. W., Johns-Krull C. M., 2014, ApJ, 797, 112
Cidale L., Zorec J., Tringaniello L., 2001, A&A, 368, 160
Coulson I. M., Walther D. M., 1995, MNRAS, 274, 977
Dahm S. E., Simon T., 2005, ApJ, 129, 829
de Winter D., van den Ancker M. E., Maira A., Thé P. S., Djie H. R. E. T. A., Redondo I., Eiroa C., Molster F. J., 2001, A&A, 380, 609
de Zeeuw P. T., Hoogerwerf R., de Bruijne J. H. J., Brown A. G. A., Blaauw A., 1999, ApJ, 117, 354
Donehew B., Brittain S., 2011, ApJ, 141, 46
Drew J. E., Busfield G., Hoare M. G., Murdoch K. A., Nixon C. A., Oudmaijer R. D., 1997, MNRAS, 286, 538
Duchêne G., 2015, Ap&SS, 355, 291
Dunhill A. C., 2015, MNRAS, 448, L67
Dunkin S. K., Barlow M. J., Ryan S. G., 1997, MNRAS, 286, 604
Finkenzeller U., 1985, A&A, 151, 340
Finkenzeller U., Mundt R., 1984, A&AS, 55, 109
Franco G. A. P., 1990, A&A, 227, 499
Fukagawa M., Tamura M., Itoh Y., Kudo T., Imaeda Y., Oasa Y., Hayashi S. S., Hayashi M., 2006, ApJ, 636, L153
Gahm G. F., Malmort A. M., 1980, A&A, 82, 295
Garrison L. M., Jr, 1978, ApJ, 224, 535
Ghosh P., Lamb F. K., 1979, ApJ, 232, 259
Gorti U., Hollenbach D., 2009, ApJ, 690, 1539
Grady C. A. et al., 2001, ApJ, 122, 3396
Graham J. A., 1970, ApJ, 75, 703
Gray R. O., Corbally C. J., 1993, ApJ, 106, 632
Gray R. O., Corbally C. J., 1998, ApJ, 116, 2530
Guetter H. H., 1979, ApJ, 84, 1846
Guimarães M. M., Alencar S. H. P., Corradi W. J. B., Vieira S. L. A., 2006, A&A, 457, 581
Gullbring E., Hartmann L., Briceno C., Calvet N., 1998, ApJ, 492, 323
Gullbring E., Calvet N., Muzerolle J., Hartmann L., 2000, ApJ, 544, 927
Hartmann L., Calvet N., Gullbring E., D'Alessio P., 1998, ApJ, 495, 385
Herbig G. H., 1960, ApJS, 4, 337
Herbig G. H., 2005, ApJ, 130, 815
Herbst W., Racine R., 1976, ApJ, 81, 840
Herbst W., Shevchenko V. S., 1999, ApJ, 118, 1043
Herczeg G. J., Hillenbrand L. A., 2008, ApJ, 681, 594
Herczeg G. J., Cruz K. L., Hillenbrand L. A., 2009, ApJ, 696, 1589
Hernández J., Calvet N., Briceño C., Hartmann L., Berlind P., 2004, ApJ, 127, 1682
Hernández J., Calvet N., Hartmann L., Briceño C., Sicilia-Aguilar A., Berlind P., 2005, ApJ, 129, 856
Hilton J., Lahulla J. F., 1995, A&AS, 113, 325
Hinkley S. et al., 2013, ApJ, 763, L9
Houk N., 1982, Michigan Catalogue of Two-dimensional Spectral Types for the HD stars. Vol. 3. Declinations −40 to −26. University of Michigan, MI
Houk N., Cowley A. P., 1975, University of Michigan Catalogue of Two-dimensional Spectral Types for the HD stars. Vol. I. Declinations −90 to −53. University of Michigan, MI
Houk N., Smith-Moore M., 1988, Michigan Catalogue of Two-dimensional Spectral Types for the HD Stars. Vol. 4, Declinations −26 to −12. University of Michigan, MI
Hubrig S. et al., 2009, A&A, 502, 283
Ingleby L. et al., 2013, ApJ, 767, 112
Jenniskens P., Desert F.-X., 1994, A&AS, 106, 39
Johns-Krull C. M., 2007, ApJ, 664, 975
Koenigl A., 1991, ApJ, 370, L39
Kurucz R. L., 1993, Kurucz CD-ROM. Smithsonian Astrophysical Observatory, Cambridge, MA
Levenhagen R. S., Leister N. V., 2006, MNRAS, 371, 252
Loinard L., Torres R. M., Mioduszewski A. J., Rodríguez L. F., 2008, ApJ, 675, L29
Long M., Romanova M. M., Kulkarni A. K., Donati J.-F., 2011, MNRAS, 413, 1061
Lubow S. H., D'Angelo G., 2006, ApJ, 641, 526
McCaughrean M. J., O'dell C. R., 1996, ApJ, 111, 1977
Malfait K., Waelkens C., Waters L. B. F. M., Vandenbussche B., Huygen E., de Graauw M. S., 1998, A&A, 332, L25
Mannings V., Sargent A. I., 1997, ApJ, 490, 792
Manoj P., Bhatt H. C., Maheswar G., Muneer S., 2006, ApJ, 653, 657
Meeus G., Waters L. B. F. M., Bouwman J., van den Ancker M. E., Waelkens C., Malfait K., 2001, A&A, 365, 476
Mendigutía I., Eiroa C., Montesinos B., Mora A., Oudmaijer R. D., Merín B., Meeus G., 2011a, A&A, 529, A34
Mendigutía I., Calvet N., Montesinos B., Mora A., Muzerolle J., Eiroa C., Oudmaijer R. D., Merín B., 2011b, A&A, 535, A99
Mendigutía I., Mora A., Montesinos B., Eiroa C., Meeus G., Merín B., Oudmaijer R. D., 2012, A&A, 543, A59
Mendigutía I. et al., 2013, ApJ, 776, 44
Mendigutía I., Fairlamb J., Montesinos B., Oudmaijer R. D., Najita J. R., Brittain S. D., van den Ancker M. E., 2014, ApJ, 790, 21
Mendigutía I., Oudmaijer R. D., Rigliaco E., Fairlamb J. R., Calvet N., Muzerolle J., Cunningham N., Lumsden S. L., 2015, preprint (arXiv:e-prints)
Miroshnichenko A. S., Gray R. O., Vieira S. L. A., Kuratov K. S., Bergner Y. K., 1999, A&A, 347, 137
Miroshnichenko A. S., Gray R. O., Klochkova V. G., Bjorkman K. S., Kuratov K. S., 2004, A&A, 427, 937
Modigliani A. et al., 2010, Proc. SPIE, 7737, 773728
Montesinos B., Eiroa C., Mora A., Merín B., 2009, A&A, 495, 901
Mora A. et al., 2001, A&A, 378, 116
Munari U., Sordo R., Castelli F., Zwitter T., 2005, A&A, 442, 1127
Muzerolle J., D'Alessio P., Calvet N., Hartmann L., 2004, ApJ, 617, 406
Muzerolle J., Luhman K. L., Briceño C., Hartmann L., Calvet N., 2005, ApJ, 625, 906
Natta A., Testi L., Randich S., 2006, A&A, 452, 245
Oudmaijer R. D. et al., 2001, A&A, 379, 564
Pérez M. R., McCollum B., van den Ancker M. E., Joner M. D., 2008, A&A, 486, 533
Pogodin M. A., Hubrig S., Yudin R. V., Schöller M., González J. F., Stelzer B., 2012, Astron. Nachr., 333, 594
Preibisch T., Mamajek E., 2008, in Reipurth B., ed., ASP Monograph Publications, Handbook of Star Forming Regions, Vol. II: The Nearest OB Association: Scorpius-Centaurus (Sco OB2). Astron. Soc. Pac., San Francisco, p. 235
Reipurth B., Zinnecker H., 1993, A&A, 278, 81
Rigliaco E., Natta A., Testi L., Randich S., Alcalà J. M., Covino E., Stelzer B., 2012, A&A, 548, A56
Salpeter E. E., 1955, ApJ, 121, 161
Sanduleak N., Stephenson C. B., 1973, ApJ, 185, 899
Shevchenko V. S., Ezhkova O. V., Ibrahimov M. A., van den Ancker M. E., Tjin A Djie H. R. E., 1999, MNRAS, 310, 210
Shu F., Najita J., Ostriker E., Wilkin F., Ruden S., Lizano S., 1994, ApJ, 429, 781
Sicilia-Aguilar A., Henning T., Hartmann L. W., 2010, ApJ, 710, 597
Simon T., Ayres T. R., Redfield S., Linsky J. L., 2002, ApJ, 579, 800
Stephenson C. B., Sanduleak N., 1971, Publ. Warner Swasey Obs., 1, 1
Strom S. E., Strom K. M., Yost J., Carrasco L., Grasdalen G., 1972, ApJ, 173, 353
Thé P. S., de Winter D., Perez M. R., 1994, A&AS, 104, 315
Tilling I., Clarke C. J., Pringle J. E., Tout C. A., 2008, MNRAS, 385, 1530

Tjin A Djie H. R. E., The P. S., Andersen J., Nordstrom B., Finkenzeller U., Jankovics I., 1989, A&AS, 78, 1
Tjin A Djie H. R. E., van den Ancker M. E., Blondel P. F. C., Shevchenko V. S., Ezhkova O. V., de Winter D., Grankin K. N., 2001, MNRAS, 325, 1441
Valenti J. A., Basri G., Johns C. M., 1993, ApJ, 106, 2024
Valenti J. A., Johns-Krull C. M., Linsky J. L., 2000, ApJS, 129, 399
van den Ancker M. E., de Winter D., Tjin A Djie H. R. E., 1998, A&A, 330, 145
van den Ancker M. E., Bouwman J., Wesselius P. R., Waters L. B. F. M., Dougherty S. M., van Dishoeck E. F., 2000, A&A, 357, 325
van den Ancker M. E., Blondel P. F. C., Tjin A Djie H. R. E., Grankin K. N., Ezhkova O. V., Shevchenko V. S., Guenther E., Acke B., 2004, MNRAS, 349, 1516
van Leeuwen F., 2007, A&A, 474, 653
Vernet J. et al., 2011, A&A, 536, A105
Vieira S. L. A., Corradi W. J. B., Alencar S. H. P., Mendes L. T. S., Torres C. A. O., Quast G. R., Guimarães M. M., da Silva L., 2003, ApJ, 126, 2971
Vink J. S., Drew J. E., Harries T. J., Oudmaijer R. D., 2002, MNRAS, 337, 356
Vink J. S., Drew J. E., Harries T. J., Oudmaijer R. D., Unruh Y., 2005, MNRAS, 359, 1049
Wade G. A. et al., 2005, A&A, 442, L31
Wade G. A., Bagnulo S., Drouin D., Landstreet J. D., Monin D., 2007, MNRAS, 376, 1145
Wheelwright H. E., Oudmaijer R. D., Goodwin S. P., 2010, MNRAS, 401, 1199
Whittet D. C. B. ed., 2003, Dust in the Galactic Environment, 2nd edn. IoP Publishing, Bristol
Whittet D. C. B., Kirrane T. M., Kilkenny D., Oates A. P., Watson F. G., King D. J., 1987, MNRAS, 224, 497
Zinnecker H., Yorke H. W., 2007, ARA&A, 45, 481

APPENDIX A: PHOTOMETRY

This appendix serves as a reference source for the sample. Provided here is Table A1, which contains all of the photometry used in this

Table A1. Photometry from the literature.

Name	U (mag)	B (mag)	V (mag)	R (mag)	I (mag)	Phot ref	$T_{\rm eff}$ (K)	$T_{\rm eff}$ ref	D (pc)	D ref
UX Ori	10.94	10.71	10.34	10.12	9.88	a	8410	i	340	ap
PDS 174	13.54	13.65	12.84	12.18	11.42	b	18 700	b	340	ap
V1012 Ori	12.62	12.46	12.04	11.61	11.25	c	8600	c	340	ap
HD 34282	10.15	10.05	9.89	9.81	9.71	a	8720	i	340	ap
HD 287823	9.98	9.90	9.68	9.59	9.48	b	8720	j	340	ap
HD 287841	10.63	10.50	10.21	10.06	9.89	a	8990	i	340	ap
HD 290409	10.20	10.11	10.02	9.96	9.89	b	10 500	b	340	ap
HD 35929	8.71	8.53	8.12	7.87	7.61	a	6870	k	360	aq
HD 290500	11.41	11.35	11.04	–	–	d	8970	b	470	ap
HD 244314	10.42	10.30	10.10	9.96	9.80	b	8720	l	440	ap
HK Ori	11.72	11.79	11.41	11.05	10.66	a	8460	m	440	ap
HD 244604	9.68	9.57	9.38	9.27	9.12	a	8720	l	440	ap
UY Ori	13.38	13.16	12.79	12.56	12.19	b	10 500	b	510	ap
HD 245185	10.02	10.00	9.91	9.87	9.82	a	9520	l	440	ap
T Ori	11.38	10.98	10.43	10.10	9.63	a	8660	i	510	ap
V380 Ori	10.80	11.04	10.53	10.11	9.50	a	9230	n	510	ap
HD 37258	9.84	9.80	9.67	9.59	9.49	a	8970	o	510	ap
HD 290770	9.18	9.30	9.27	9.23	9.18	b	10 500	b	470	ap
BF Ori	10.34	10.05	9.82	9.68	9.48	a	8990	i	510	ap
HD 37357	9.00	8.95	8.84	8.79	8.72	a	9230	l	510	ap
HD 290764	10.29	10.20	9.88	9.68	9.44	b	7200	b	470	ap
HD 37411	10.07	9.95	9.82	9.72	9.58	a	9100	l	510	ap
V599 Ori	17.07	15.41	13.76	12.69	11.55	a	7200	b	510	ap
V350 Ori	11.39	11.15	10.82	10.62	10.34	a	8990	i	510	ap
HD 250550	9.34	9.61	9.54	9.32	9.54	e	10 750	l	280	ar
V791 Mon	10.31	10.68	10.38	10.12	9.87	b	18 700	p	1100	as
PDS 124	13.15	12.97	12.44	12.15	11.81	b	9520	b	830	w
LkHa 339	14.59	14.24	13.47	12.80	11.93	a	9230	q	830	w
VY Mon	15.28	14.56	12.97	11.82	10.60	a	8200	i	800	at
R Mon	12.17	12.53	11.93	11.41	10.87	a	12 400	i	800	at
V590 Mon	12.52	12.75	12.60	12.42	12.12	a	13 000	r	800	at
PDS 24	13.94	13.62	13.26	12.98	12.69	b	10 500	b	590	ap
PDS 130	14.42	14.06	13.40	12.96	12.44	b	10 500	b	830	w
PDS 229N	13.82	13.70	13.13	12.74	12.24	b	9520	b	830	w
GU CMa	5.88	6.56	6.54	6.47	6.37	a	25 000	s	1050	au
HT CMa	12.55	12.29	11.87	11.38	11.87	e	9520	q	1050	au
Z CMa	11.20	10.50	9.25	8.40	7.65	f	30 000	f	1050	au
HU CMa	11.72	11.84	11.55	11.32	11.16	a	11 900	q	1050	au
HD 53367	6.80	7.37	6.95	6.67	6.30	a	29 500	s	1050	au
PDS 241	12.33	12.71	12.06	11.45	11.11	b	30 000	b	7000	av
NX Pup	9.93	9.96	9.63	9.38	9.07	a	7290	t	410	ap
PDS 27	14.61	14.32	13.00	12.00	10.98	b	17 500	u	2900	u
PDS 133	13.57	13.61	13.13	12.79	12.50	b	14 000	b	2500	b

Table A1 – *continued.*

Name	U (mag)	B (mag)	V (mag)	R (mag)	I (mag)	Phot ref	$T_{\rm eff}$ (K)	$T_{\rm eff}$ ref	D (pc)	D ref
HD 59319	7.86	8.23	8.31	8.34	8.42	a	11 900	v	–	–
PDS 134	12.50	12.61	12.20	11.92	11.65	b	14 000	b	–	–
HD 68695	10.00	9.92	9.82	9.76	9.66	b	9520	w	410	ap
HD 72106	8.39	8.50	8.50	8.49	8.49	b	9810	x	370	ap
TYC 8581-2002-1	12.18	11.94	11.48	11.19	10.95	b	8200†	b	145	ap
PDS 33	12.85	12.63	12.34	12.16	11.97	b	9520	b	370	ap
HD 76534	7.68	8.18	8.07	7.97	7.84	a	20 350	y	370	ap
PDS 281	9.43	9.46	8.87	8.50	8.08	b	17 050	b	370	ap
PDS 286	14.39	13.91	12.15	10.91	9.76	b	30 000	b	370	ap
PDS 297	12.50	12.34	12.03	11.83	11.59	b	7850	b	145	ap
HD 85567	8.11	8.65	8.51	8.33	8.08	a	12 450	z	650	aq
HD 87403	9.28	9.31	9.26	9.22	9.16	b	10 100	aa	145	ap
PDS 37	15.56	15.06	13.54	12.38	11.21	b	17 500	u	3700	u
HD 305298	10.36	11.07	10.86	10.66	10.47	b	36 900	ab	–	–
HD 94509	9.01	9.15	9.12	9.10	9.10	a	9730	ac	–	–
HD 95881	8.53	8.36	8.19	–	–	g	8990	ad	118	ap
HD 96042	7.89	8.60	8.47	8.36	8.23	b	25 400	ad	–	–
HD 97048	8.96	8.80	8.44	8.20	7.95	a	10 010	ae	160	aq
HD 98922	6.74	6.82	6.77	6.69	6.61	a	10 500	w	850	aq
HD 100453	8.10	8.07	7.78	7.60	7.42	b	7390	aa	122	aq
HD 100546	6.60	6.70	6.69	6.67	6.66	a	10 500	af	97	aq
HD 101412	9.57	9.42	9.24	9.13	9.00	b	10 010	aa	118	ap
PDS 344	13.09	13.40	13.15	12.95	12.77	b	15 400	b	–	–
HD 104237	6.64	6.73	6.52	6.38	6.23	a	8410	z	115	aq
V1028 Cen	10.39	10.70	10.61	10.48	10.33	a	14 100	z	130	aq
PDS 361S	13.10	13.35	12.85	12.49	12.09	b	18 700	b	–	–
HD 114981	6.55	7.13	7.23	7.27	7.33	b	15 400†	b	550	aq
PDS 364	13.85	13.93	13.46	13.05	12.63	b	11 900	ag	118	ap
PDS 69	9.92	10.12	9.80	9.50	9.12	b	17 050	ah	630	ah
DG Cir	15.96	15.87	14.75	13.96	13.06	a	15 000	ai	700	aw
HD 132947	8.87	8.96	8.91	8.89	8.89	a	10 500	af	–	–
HD 135344B	9.14	9.14	8.63	8.16	7.83	h	6590	aj	140	ap
HD 139614	8.67	8.64	8.40	8.26	8.11	b	7850	aj	140	ap
PDS 144S	13.59	13.28	12.79	12.49	12.16	b	8200	b	1000	b
HD 141569	7.23	7.20	7.10	7.03	6.95	a	9520	aj	116	aq
HD 141926	8.72	9.20	8.64	8.21	7.77	b	20 300	b	–	–
HD 142666	9.42	9.17	8.67	8.35	8.01	b	7580	aj	145	ap
HD 142527	9.20	9.15	8.27	–	–	g	6260	ak	140	ak
HD 144432	8.64	8.53	8.17	7.94	7.72	a	7350	i	160	aq
HD 144668	7.28	7.11	6.78	6.57	6.38	a	7930	al	160	aq
HD 145718	10.00	9.62	9.10	8.79	8.45	b	8200	ag	145	ax
PDS 415N	13.43	12.96	12.04	11.47	10.85	b	7200	b	120	ay
HD 150193	9.69	9.33	8.80	8.41	7.97	a	10 010	af	120	ay
AK Sco	9.56	9.53	8.90	8.54	8.18	a	6450	am	130	aq
PDS 431	14.20	13.99	13.42	13.02	12.59	b	9520	b	145	ap
KK Oph	13.17	12.97	12.36	11.83	11.03	a	8030	an	145	ap
HD 163296	7.00	6.96	6.85	6.80	6.71	a	8720	l	119	aq
MWC 297	14.94	14.27	12.03	10.18	8.80	a	23 700	ao	250	ao

†These two stars are listed as objects QT3 (TYC 8581-2002-1) and QT4 (HD 114981) in the first table of Vieira et al. (2003). However, their places appear swapped in the second table by these authors. This swap is supported by additional photometry of HD 114981 and by the authors' observed temperatures and the temperatures derived in this work. Based on this, we have swapped the photometry from Vieira et al. (2003) around for these two stars. References: (a) de Winter et al. (2001), (b) Vieira et al. (2003), (c) Miroshnichenko et al. (1999), (d) Guetter (1979), (e) Herbst & Shevchenko (1999), (f) van den Ancker et al. (2004), (g) Malfait et al. (1998), (h) Coulson & Walther (1995), (i) Mora et al. (2001), (j) Hernández et al. (2005), (k) Miroshnichenko et al. (2004), (l) Gray & Corbally (1998), (m) Baines et al. (2004), (n) Finkenzeller & Mundt (1984), (o) Gray & Corbally (1993), (p) Cidale, Zorec & Tringaniello (2001), (q) Hernández et al. (2004), (r) Pérez et al. (2008), (s) Tjin A Djie et al. (2001), (t) Finkenzeller (1985), (u) Ababakr et al. (2015), (v) Houk & Smith-Moore (1988), (w) Herbst & Racine (1976), (x) Houk (1982), (y) Valenti, Johns-Krull & Linsky (2000), (z) van den Ancker, de Winter & Tjin A Djie (1998), (aa) Guimarães et al. (2006), (ab) Graham (1970), (ac) Stephenson & Sanduleak (1971), (ad) Houk & Cowley (1975), (ae) Whittet et al. (1987), (af) Levenhagen & Leister (2006), (ag) Carmona et al. (2010), (ah) Reipurth & Zinnecker (1993), (ai) Gahm & Malmort (1980), (aj) Dunkin, Barlow & Ryan (1997), (ak) Fukagawa et al. (2006), (al) Tjin A Djie et al. (1989), (am) Andersen et al. (1989), (an) Herbig (2005), (ao) Drew et al. (1997), (ap) de Zeeuw et al. (1999), (aq) van Leeuwen (2007), (ar) Canto et al. (1984), (as) Hilton & Lahulla (1995), (at) Dahm & Simon (2005), (au) Shevchenko et al. (1999), (av) Avedisova (2000), (aw) Franco (1990), (ax) Preibisch & Mamajek (2008), (ay) Loinard et al. (2008).

work, along with references to the sources. Additionally, previously assigned literature values of distance and temperature are included for the whole sample (where possible, some do not have previous distance estimates).

APPENDIX B: EXCEPTIONAL STARS

Seven of the stars in the sample cannot be assigned a temperature from the spectra alone (see Section 3.1). For these objects, a different approach must be undertaken on an individual basis in order to assign a limiting temperature. This is done by drawing upon as many literature sources on these objects as possible. Fortunately, there are very few objects in the sample which require this specialist treatment. The stars and steps taken towards them are detailed below.

VY Mon – This star is included here because it has the worst SNR of the sample. This makes accurate spectral typing difficult, but a cautious estimate of around 12 000 K can be made for the temperature. This agrees with literature estimates of 8200–12 000 K (Mora et al. 2001; Manoj et al. 2006). A generous error of 4000 K is adopted.

R Mon – In the spectra of R Mon all lines are seen in emission or as P-Cygni profiles, making any temperature estimate impossible from spectra alone. The temperature has been previously listed as around 12 000 K in past works (Mora et al. 2001; Manoj et al. 2006). We adopt this literature temperature.

Z CMa – This star has lots of P-Cygni and emission lines in its spectra, but lacks absorption features for spectral typing. Again we must turn to the literature. In the literature, this star is seen to have the largest spread in listed temperatures: ranging from 30 000 K (van den Ancker et al. 2004; Manoj et al. 2006), down to 11 500 K (Donehew & Brittain 2011) and 8500 K (Hinkley et al. 2013). We choose to adopt, and test, the most recent temperature from Hinkley et al. (2013). This is because their work spatially resolves the Herbig star in this system from its FU Or-like companion. In addition to this, they provide SED fitting to the observed photometry to determine the temperature.

PDS 27 and PDS 37 – These two objects display very strong emission and P-Cygni profiles. They are also the focus of a recent paper by Ababakr et al. (2015) who determine distances and stellar parameters of the objects. We adopt their stellar parameters and distances in our work as they follow a similar methodology. The temperature they found of ∼21 000 K, for both objects, is in agreement with the values found by Vieira et al. (2003).

PDS 133 – Another star devoid of any photospheric absorption in its spectra, and has extremely strong emission lines (the equivalent width of Hα is ∼−100 Å). Therefore, using the spectra to assign a temperature is impossible. For this reason, we adopt a temperature around 14 000 K, based on the literature (Vieira et al. 2003).

DG Cir – Another star with reasonably strong emission; the Balmer series are seen as P-Cygni profiles. A broad spectral type of class B has previously been assigned to this star by Sanduleak & Stephenson (1973) and Vieira et al. (2003). Gahm & Malmort (1980) do not give a spectral type but note its similarities to V380 Ori. A small indication of absorption lines can be seen around 5200 Å, but they appear close to many emission lines making an exact temperature determination difficult. We therefore agree with a B spectral type, and based on the absorption would narrow this to a late-B-type star of ∼11 000 K, with a generous error of 3000 K.

This paper has been typeset from a TEX/LATEX file prepared by the author.